

Contribution of local and remote anthropogenic aerosols to a record-breaking torrential rainfall event in Guangdong province, China

Z. Liu^{1,2,3}, Y. Ming⁵, C. Zhao⁶, N.C. Lau^{1,2,4}, J.P. Guo⁷, M. Bollasina³, Steve H.L. Yim^{1,4,2}

¹Institute of Space and Earth Information Science, The Chinese University of Hong Kong, Hong Kong, China

5 ²Institute of Environment, Energy and Sustainability, The Chinese University of Hong Kong, Sha Tin, N.T., Hong Kong

³School of Geosciences, University of Edinburgh, UK

⁴Department of Geography and Resource Management, The Chinese University of Hong Kong, Sha Tin, N.T., Hong Kong

⁵Geophysical Fluid Dynamics Laboratory/NOAA, Princeton, New Jersey, USA

⁶School of Earth and Space Sciences, University of Science and Technology of China, Hefei, Anhui, China

10 ⁷State Key Laboratory of Severe Weather, Chinese Academy of Meteorological Sciences, Beijing 100081, China

Correspondence to: Steve H.L. Yim (steveyim@cuhk.edu.hk)

Abstract. A torrential rainfall case, which happened in Guangdong Province during December 14–16, 2013, broke the historical rainfall record in the province in terms of duration, affected area, and accumulative precipitation. The influence of anthropogenic aerosols on this extreme rainfall event was examined using a coupled meteorology-chemistry-aerosol model.

15 Enhancement of precipitation in the estuary and near the coast up to 33.7 mm was mainly attributed to aerosol-cloud interactions, whereas aerosol-radiation interactions partially compensated 14% of the precipitation increase. Further analysis of different hydrometeors and latent heat sources suggests that the ACI effects on intensifying the precipitation can be divided into two stage: cold rain enhancement in the former stage while warm rain in the latter. Responses of precipitation to changes in anthropogenic aerosols concentrations from local (i.e., Guangdong province) and remote (i.e., outside Guangdong province)

20 sources were also investigated through simulations with reduced aerosol emissions from either local or remote sources. Accumulated aerosol concentration from local sources aggregated mainly near the surface and diluted quickly after the precipitation initiated. By contrast, aerosol concentration from remote emissions extended up to 8 km and lasted much longer before decreasing until peak rainfall began, because aerosols were continuously transported by the strong northerly. The patterns of precipitation response to remote and local aerosols concentrations resembled each other. However, compared with

25 local aerosols through warm rain enhancement, remote aerosols contributed more than twice the precipitation increase via intensifying both cold and warm rain, occupying a predominant role. Ten times of the emission sensitivity test resulted in about ten times of PM_{2.5} concentration compared with the control run. Warm rain is drastically suppressed in 10× run. The patterns of precipitation and cloud property changes also resembled that in the control run, but with much greater magnitude. The precipitation average over Guangdong province decreased by 1.0 mm but increased by 1.4 mm in the control run. We noted

30 that the reinforced precipitation increase was concentrated within a more narrowed downstream region, whereas the precipitation decrease was more dispersed across the upstream region. This indicates that the excessive aerosols not only suppress rainfall but also change the spatial distribution of precipitation, increasing the rainfall range, thereby potentially exacerbating flood and drought elsewhere. This study highlights the importance of considering aerosols in meteorology to

improve extreme weather forecasting. Furthermore, aerosols from remote emissions may outweigh those from local emissions in the cloud invigoration effect.

1 Introduction

5 Synoptic weather is a key factor driving air pollution events through photochemical, turbulence, wet deposition, and transport processes (Ding et al., 2009; Guo et al., 2017; Liu et al., 2001; Madronich, 1987). Numerous studies have forecast air quality either numerically or statistically based on weather conditions (Dutot et al., 2007; Otte et al., 2005). In recent years, more and more efforts have been made to identify the influence of aerosols on synoptic weather (Ding et al., 2013; Grell et al., 2011), particularly on different types of extreme weather, such as tropical cyclone (Wang et al., 2014; Zhao et al., 2018), hail storm (Iltoviz et al., 2016), and extreme rainfall (Fan et al., 2015; Zhong et al., 2015).

10 For decades, China has been affected by severe air pollution due to rapid urbanization and economic development (He et al., 2002). The Pearl River Delta (PRD) region, situated on the south coast of China, is one of the most developed as well as the most polluted region. The aerosol optical depth retrieved from the Moderate Resolution Imaging Spectroradiometer is typically higher than 0.6 in Guangzhou, a megacity in the PRD region (Wu et al., 2005).

In addition to reducing visibility and inducing respiratory diseases (Cohen et al., 2015; Gu and Yim, 2016; Chen et al., 2017), 15 high aerosol concentrations can also affect weather and climate through interactions with radiation and clouds (Bollasina et al., 2011; Lau and Kim, 2006; Wang et al., 2011). Aerosols absorb and scatter solar radiation and serve as cloud condensation nuclei and ice nuclei, which are referred to as aerosol-radiation interactions (ARI) and aerosol-cloud interactions (ACI), respectively (IPCC, 2013). Both ARI and ACI influence convection and hence precipitation (Fan et al., 2008, 2013; Koren et al., 2004; Liu et al., 2018; Rosenfeld et al., 2008; Fan et al., 2018). Liu et al. (2018) found that ARI suppressed deep convection 20 by reducing the relative humidity in the middle-upper troposphere and by weakening the upward motion. Fan et al. (2015) revealed that ARI weakened convergence, enhanced atmospheric stability, and suppressed convection in the basin during the daytime. Excess moist static energy was transported to the mountains, generating heavy rainfall at night. This local rainfall suppression effect is dramatically modulated by the synoptic-scale forcing (Zhong et al., 2017). The effects of ACI on deep convection and precipitation have received more attention and are more controversial in both observational and modeling 25 studies compared to those due to ARI. Increased aerosols can suppress or enhance precipitation depending on environmental conditions such as humidity, cloud type, cloud phase, and vertical wind shear (Khain, 2009; Lee et al., 2008; Tao et al., 2012). Khain (2009) and Fan et al. (2007) reported that increases in humidity generate more condensate, resulting in more precipitation from deep convective clouds, especially in a polluted environment. Studies have reported that aerosols inhibit precipitation from shallow clouds (Andreae et al., 2004; Chen et al., 2016; Rosenfeld, 2000), whereas they invigorate deep 30 convection with warm ($>15^{\circ}\text{C}$) cloud bases (Bell et al., 2008; Koren et al., 2010, 2014). By contrast, smaller cloud droplets induced by aerosols could remain liquid near or above 0°C when lacking ice nuclei, inhibiting precipitation (Cui et al., 2006; Rosenfeld and Woodley, 2000). Fan et al. (2009, 2012) suggested that increased aerosols enhanced convection under weak

wind shear and suppressed convection under strong wind shear by increasing evaporative cooling in an isolated storm. However, the evaporative cooling induced by aerosols has also been found to enhance precipitation under strong wind shear in cloud systems (Lee et al., 2008; Tao et al., 2007). Most of these works attribute the convection invigoration effect to cold cloud processes accompanied by latent heat release due to freezing. Recently, Fan et al. (2018) found that the latent heat release could be mainly attributed to condensational heating rather than ice-related processes at upper levels, differing from cold-cloud invigoration (Rosenfeld et al., 2008).

A competition between ARI and ACI has been found at both cloud-resolving (Lin et al., 2017; Wang et al., 2018) as well as regional (Wang et al., 2016) scales. Fan et al. (2008) suggested that the ARI-induced rainfall suppression can outweigh the invigoration effects in deep convective systems as the absorption of aerosols enhances. Koren et al. (2008) showed that the net effect of two opposite influences on clouds over the Amazon depends on the initial cloud fraction. Large cloud cover fractions were mostly invigorated by ACI, whereas small cloud cover fractions were suppressed by ARI. The net aerosol effect on deep convection, and the overall invigoration or suppression, depends also on the aerosol type as different aerosol species have different radiative and microphysical properties (Jiang et al., 2018). Previous studies have focused on role of aerosols on summer extreme rainfall cases (Fan et al., 2015; Zhong et al., 2015) because most extreme rainfall events occur in summer over China (Fu et al., 2013).

We selected a wintertime torrential rainfall event, which broke the record of Guangdong Province since 1951 in terms of duration, affected area, and cumulative rainfall over the PRD region, to further understand the combined effects and relative importance of ARI and ACI on precipitation. Before this heavy rainfall, the PRD region was affected by strong haze with $PM_{2.5}$ concentrations approaching $174 \mu g m^{-3}$. The significant transboundary nature of air pollution in China has been well recognized (e.g., Gu and Yim, 2016). The effects of local and remote aerosol emissions on long-term changes in monsoons and associated precipitation, particularly the Indian summer monsoon, have been examined in recent years (Bollasina et al., 2014; Cowan and Cai, 2011; Guo et al., 2016b; Li et al., 2016; Jin et al., 2016). Yet, the effects of local and remote aerosol emissions on extreme rainfall events remain mostly unexplored. Moreover, given the strong monsoonal flow and severe air pollution over northeastern China (Figure S1b), the regional aerosol loading could be either from local emissions or transport by prevailing northeasterly. A critical question, therefore, is whether aerosol concentrations that affected this extreme rainfall case originated from local or remote aerosol emission sources. The remainder of this study is organized as follows: Section 2 describes the model used, the experimental design as well as the observational datasets. The effects of aerosols on the simulated extreme rainfall event are discussed in section 3. The main conclusions are summarized and discussed in section 4.

2 Model configurations, experiment set-up, and observational datasets

The main tool used in this work was the Weather Research and Forecasting (WRF) model coupled with Chemistry (WRF-Chem) v3.5.1 (Grell et al., 2005), with some recent improvement by the University of Science and Technology of China (Zhao et al., 2013a, 2014, 2016; Hu et al., 2016). The details of the WRF-Chem configuration are documented in section 2.1, followed

by a description of model experimental design in section 2.2. The observational datasets used to validate the model are described in section 2.3.

2.1 WRF-Chem

WRF-Chem is a regional weather and climate model coupled with gas-phase chemistry mechanisms and aerosol physiochemical modules. In this model, chemical and meteorological components use the same grid coordinates, time steps, transport schemes, and subgrid physics. The meteorological component (WRF) uses an Eulerian dynamical core with a nonhydrostatic solver (Skamarock et al., 2008). Gas-phase chemical reactions are estimated using the carbon bond chemical mechanism (Zaveri and Peters, 1999). Aerosol physics and chemistry are treated using the Model for Simulating Aerosol Interactions and Chemistry (MOSAIC) scheme (Zaveri et al., 2008) with aqueous chemistry. The aerosol size distribution is represented by four discrete size bins within MOSAIC: 0.039–0.156 μm , 0.156–0.625 μm , 0.625–2.5 μm , and 2.5–10 μm (Fast et al., 2006). A aerosol dry deposition is based on Binkowski and Shankar (1995), while in-cloud (rainout) and below-cloud (washout) removal of aerosols by resolved clouds and precipitation are simulated following Easter et al. (2004) and Chapman et al. (2009), respectively. The transport and wet removal of aerosols by convective clouds are also considered using the Kain–Fritsch (KF) scheme (Kain and Fritsch, 1990) following Zhao et al. (2009, 2013b). The major physical components of the meteorological module comprise the KF cumulus scheme; the Yonsei University (YSU) planetary boundary layer (PBL) scheme (Hong et al., 2006); the National Center for Environmental Prediction, Oregon State University, Air Force, and Hydrologic Research Lab’s (NOAH) land surface model (Chen and Dudhia, 2001); the Morrison two-moment scheme for cloud microphysics (Morrison et al., 2009); and the rapid radiative transfer for global (RRTMG) for both longwave and shortwave radiation schemes (Iacono et al., 2008). Aerosol interactions with shortwave and longwave radiation are incorporated into the model by linking aerosol optical properties, including optical depth, single-scattering albedo, and asymmetry factor, to RRTMG shortwave and longwave schemes, respectively (Zhao et al., 2010, 2011). The effects of ACI are estimated by considering the activation of aerosols to form cloud droplets based on the maximum supersaturation in the Morrison microphysical scheme (Chapman et al., 2009; Yang et al., 2011).

2.2 Experimental design

A set of WRF-Chem simulations are conducted to investigate the effect of aerosols on the extreme rainfall event of December 14–16, 2013. Unless specified, time in this study refers to local standard time (LST), which is equal to UTC+8. Two nested simulations (one-way nesting) are run at a horizontal resolution of 20 km and 4 km, respectively, for a domain covering most of China (87.47°–131.67° E, 11.42°–41.22° N) and the Guangdong province (109.59°–117.32° E, 20.07°–25.62° N) (Figure S1a). The cumulus scheme is turned off in the inner domain. Both nested grids use 41 vertical levels extending from the surface to 100 hPa. The meteorological initial and boundary conditions (ICs and BCs) are derived from the 6-hourly data from National Center for Environmental Prediction global final analysis with a horizontal resolution of $1^\circ \times 1^\circ$. The 6-hourly chemical ICs and BCs are generated from the Model for Ozone and Related Chemical Tracer version 4 (MOZART-4), which is an offline

global chemical transport model suited for tropospheric studies, at a horizontal resolution of $1.9^\circ \times 2.5^\circ$ with 56 vertical levels (Emmons et al., 2010). Anthropogenic emissions are obtained from the Emissions Database for Global Atmospheric Research Hemispheric Transport of Air Pollution v2 inventory (Janssens-Maenhout et al., 2015) for the year 2010 with a resolution of $0.1^\circ \times 0.1^\circ$ (http://edgar.jrc.ec.europa.eu/htap_v2/). Biomass burning emission data are extracted from Fire INventory from NCAR version 1.5 (Wiedinmyer et al., 2010). Dust and sea salt emission schemes are updated following Zhao et al. (2010) and Zhao et al. (2013a), respectively. The results show marginal differences between simulations with and without dust and sea salt emissions (figure not shown) in our study case; possible reasons for this are discussed in section 4.

Six sets of experiments are performed (Table 1). To isolate robust signals from the model's natural variations, five ensemble members with perturbed ICs at 3-h intervals are conducted for each experiment. The simulations started from 08Z to 20Z on December 13 with 3-h intervals, and all end at 02Z on December 17 in 2013. Data up to December 14 is for model spin up, and the following analysis focuses on the period during December 14–16. The control experiment (CTL) uses current emissions and both ARI and ACI effects are enabled (Table 1). Following Fan et al. (2015), we scale anthropogenic and fire emissions to represent background aerosols before the extensive economic development in China and perform the CLEAN simulation; a scaling factor of 0.1, instead of 0.3 as in Fan et al. (2015), is chosen to account for the larger 2010 emissions than those in 2006 (Chang et al., 2018). The difference between CTL and CLEAN represents the total effects of aerosols including both ARI and ACI effects. To examine the role and relative importance of ARI and ACI, the ARIoff run is conducted by excluding the ARI effect in the CTL experiment. Thus, the difference between CTL and ARIoff represents ARI effects (Zhong et al., 2015). The ACI effects are approximated by looking at the difference between CTL – CLEAN and CTL – ARIoff. To distinguish and isolate the effects induced by local (i.e., domain 2, aerosol sources within Guangdong province) emissions and remote (i.e., domain 1, sources located outside Guangdong province) emissions, we conduct two other experiments, identical to CTL, except for scaling the emissions and chemical ICs and BCs by a factor of 0.1 in domain 2 (hereafter D1 run, Table 1) and domain 1 (hereafter D2 run), respectively. Note that the offline chemical BCs extracted from MOZART are only applicable to domain 1. Along with CTL, these experiments allow us to separate aerosol-related changes that would have occurred with either local or remote aerosol emissions by examining the difference between CTL minus CLEAN and either D2 minus CLEAN or D1 minus CLEAN, respectively. To test sensitivity of the results to the magnitude of aerosol emissions, we perform an additional experiment in which the emissions and chemical ICs and BCs (i.e., as in CTL) are scaled by a factor of 10 ($10\times$).

2.3 Observational datasets

The performance of model-simulated precipitation is evaluated with satellite-based precipitation products and in-situ rainfall observations.

Climate Prediction Center morphing technique (CMORPH) dataset produced by the National Oceanic and Atmospheric Administration covering the period from December 2002 to present are used. In this technique, infrared geostationary satellites observe the motion vectors of precipitation patterns to generate half-hourly precipitation estimates by using passive microwave (PMW) sensors. Time-weighted linear interpolation is exploited to morph the shape and intensity of precipitation features

when and where PMW data are unavailable. This provides data for global (60° S–60° N) precipitation analysis with a horizontal resolution of 0.07277° (approximately 8 km at the equator) and temporal resolution of 30 minutes. More details of the CMORPH product are documented by Joyce et al. (2004).

5 In-situ hourly precipitation dataset is developed at the National Meteorological Information Center of the China Meteorological Administration (source: <http://data.cma.cn>). A total of 115 stations are within domain 2. Their locations are represented as colored circles in Figure 2a.

10 The ERA-Interim reanalysis is used to evaluate the model performance in simulating the large-scale circulation. This data is a global atmospheric reanalysis provided by the European Centre for Medium-Range Weather Forecasts (ECMWF) (Dee et al., 2011). The data is available from 1979 onward at a horizontal resolution of approximately 0.25° which is comparable to the resolution of domain 1.

The hourly PM_{2.5} concentration in-situ dataset is used to evaluate the model performance on PM_{2.5} concentration. This dataset is obtained from the website of the Ministry of Environmental Protection (source: <http://106.37.208.233:20035>) (Zhang and Cao, 2015). In total, 58 stations are within domain 2. Their locations are denoted as colored circles in Figure 1c.

3 Results

15 A rare continuous rainstorm occurs during December 14–16, 2013 over all of Guangdong Province. The 3-day accumulated rainfall at most stations exceeded 100 mm (Figure 2a), which may benefit winter and spring water usage, promote air cleaning, and reduce forest fire risk. This is the most extreme precipitation event in the province in terms of duration, affected area, and cumulative rainfall in December since the meteorological record of Guangdong province set in 1951 (Deng et al., 2015). The mid-tropospheric flow pattern, with a ridge to the northeast of the Tibet Plateau and a trough over the west of the Indo-China Peninsula, is favorable for cold air moving southward, whereas moist and warm air from the Bay of Bengal and the South China Sea move northward (see Figure S2). This pattern results in strong convergence at lower levels over domain 2 (Figure 20 1b), leading to intense convection as indicated by the bright white color in the natural-color satellite image captured by NASA's Terra (Figure 1a). The cloud top temperature average over the land in domain 2 is lower than –15 °C almost everywhere with minimum values of –35 °C (Figure S1b). The Guangdong province is affected by severe pollution on 25 December 13, the day before the storm. The hourly-averaged PM_{2.5} concentrations exceeded 100 µg m⁻³ in the Pearl River Delta region, with a peak value of about 174 µg m⁻³ (Figure 1c). The area to the north of the Guangdong province, including the Zhejiang, Jiangsu, and Anhui provinces, is blanketed in grey haze in the satellite image (Figure 1a), indicating the presence of smog. Column-integrated PM_{2.5} concentrations in these areas, as simulated in CTL, reach up to 2000 µg m⁻² during 30 December 14–16, 2013 (Figure 1b). Strong prevailing northeasterly winds south of 30° N along the east coast of China indicate a strong monsoonal flow (Chang et al., 2006). The patterns of circulation and pollutant are favorable for aerosol transport to the south of China. Built on the observational and modeling works discussed above, we examine in section 3.2 the total effects

and relative importance of ARI and ACI on this extreme rainfall event. We also distinguish and isolate the response to local and remote aerosol emissions in section 3.3. In section 3.4, the sensitivity of precipitation to aerosol emissions is explored.

3.1 Model evaluation compared with observational datasets

5 The 500-hPa geopotential height and wind pattern simulated in the control run are evaluated with ERA-interim data (Figure S2). The model well captures the trough over the western of the Indo-China Peninsula and the sub-tropical high over the South China Sea and northwestern Pacific. The pattern correlation of the 500-hPa geopotential height reaches 0.99 at the 99% significance. The model simulated $PM_{2.5}$ concentration reproduces the main features of the observed pattern with higher concentration over mega cities and low over surrounding areas (Figure S6). The model fails to reproduce the hot spot near the estuary, possibly due to the model coarse resolution or a bias in the emissions. In the time series, both CTL and observations
10 show a dramatically decreasing trend of $PM_{2.5}$ concentrations once the rainfall initiated (Figure S7). The model could generally replicate the spatial distribution and time evolution of $PM_{2.5}$ concentrations with some underestimation during the first two days. The underestimation may be due to a two strong wash out in the CTL (Figure 2d). This bias may underestimate the aerosol impact on rainfall.

Figure 2 compares the model-simulated precipitation performance to observations. The model output and satellite retrievals
15 are interpolated to the location of in-situ observations through bilinear interpolation (Figure 2a–2c). Approximately 100 mm of precipitation accumulates during December 14–16, 2013, covering uniformly across the Guangdong Province. However, CMORPH satellite data, which is often used to evaluate model rainfall performance, underestimates the precipitation, particularly near the coast. Previous studies have reported that CMORPH products substantially underestimated heavy rainfall (Jiang et al., 2018; Qin et al., 2014) and cold season rainfall (Xie et al., 2017). The time series of the average rain rate over
20 Guangdong Province reveals a remarkable extreme rainfall event with a lasting rain rate of 2.5 mm h^{-1} on the second and third day; CMORPH data distinctly underestimates rainfall for these days (Figure 2d). The model reproduces a similar magnitude to the observations with an earlier peak in the early morning near 08Z on December 15. The initial time and physics schemes including microphysics, land surface, and PBL are tuned to check whether the peak time will be different. However, the rainfall changes are mostly happened in amplitude rather than peak time, thus we conclude that the bias may be induced by the
25 meteorology boundary conditions from global model. The Taylor diagram for 3-day accumulated rainfall in Figure 2f suggests that the model simulation yields a higher pattern correlation of 0.50–0.55 and a lower bias of 5%–20% than the CMORPH retrieval does (0.4 and >20% for pattern correlation and bias, respectively). Signs of bias are represented by inverted (negative) or upright (positive) triangles, indicating that the model overestimated the rainfall amount while the satellite products underestimates it. **The TRMM data is also used to evaluate this extreme case in Figure S5d. Precipitation is also underestimated**
30 **along the coast as well as in CMORPH data.** Overall, the model replicates the spatial distribution, time evolution, and the intensity of this extreme rainfall event. Note that all the analyses in the following sections are based on simulation results from domain 2.

3.2 Effects of ARI versus those of ACI

Aerosols can change cloud properties and precipitation through two processes, radiative and microphysical (Graf, 2004; Kaufman and Koren, 2006), which contribute to the largest uncertainty in human-induced climate changes. We attempt to isolate the effects of ARI and ACI and thus investigate their roles and relative importance in this extreme rainfall event. Figure 3 shows the spatial distribution of the daily accumulated precipitation differences for December 14 and 15 between the different scenarios. Because the results on the third day, December 16, illustrate a similar mechanism to those on December 15, our analysis focus on December 15. The differences between scenarios on December 16 are in the supplementary materials for reference (Figure S3). Distinct effects of aerosols appear during the second day when the rainfall peaked (Figure 3d), although aerosols lead to more cloud droplet number concentration associated with smaller radius on the first day (Figure 5a); this suggests that the effects of aerosols on precipitation are modulated by other factors (e.g. meteorological conditions). On December 15, the domain-averaged precipitation increases by 1.4 mm. A reduction of up to 19.4 mm appears in northern Guangdong province, whereas an increase of up to 33.7 mm occurs in southern Guangdong province, particularly in the region near the Pearl River estuary and land along the coast. The region 22° – 24° N and 112° – 115° E, denoted by red boxes in Figure 3, is our focus for the following analysis, because it exhibits prominent rainfall increases by 16.7% (+7.8 mm) on average and covers some of the most advanced city clusters in China including Hong Kong, Shenzhen, and Guangzhou. The corresponding precipitation differences induced by ARI and ACI are -1.3 mm (-2.8%) and $+9.3$ mm ($+19.9\%$), respectively. Positive indicates an increase, and negative indicates a decrease. It is evident that from the pattern of precipitation changes that the net aerosol effects are dominated by ACI during this event. The time series of average precipitation over the red box shows that the model simulations reproduce a rainfall amount comparable to the observation (Figure S4). Compared with the CTL and ARIoff runs, the CLEAN run yields an analogous time evolution, with less rainfall during the peak time from 06Z on December 15 to 10Z on December 16. The next question that arose is how ACI can increase the rainfall amount over the region. Figure 4a shows the time-height cross section of cloud fraction (shading) and $PM_{2.5}$ concentration (contour) in the CTL run. Most cloud fraction concentrates below 8 km in the first day, associating with small amount of rainfall. Deep convection, with a cloud base at approximately 500 m and cloud top extending to approximately 1 km, appears during December 15–16 when peak rainfall occurs. The $PM_{2.5}$ concentrations in Figure 4a portray a sharp contrast before and after the rainfall peak. After the rainfall peaked at near 07Z in Figure S3, aerosols are washed out dramatically by precipitation. However, before the peak, $PM_{2.5}$ concentrations decrease gradually from $40 \mu\text{g m}^{-3}$ near the surface to $5 \mu\text{g m}^{-3}$ near 7 km above ground. With aerosols acting as cloud condensation nuclei, more cloud droplets are formed with smaller radius, particularly before the rainfall peak when aerosol concentration is high (Figure 5a). Smaller cloud droplets evaporate associated with a reduction of cloud water (Figure 6a), resulting in cooling effect and weaker updraft (Figure 5g and 5i). Thus, the cloud fraction decreases before the peak, especially below 2 km. By contrast, there was a prominent cloud fraction band increase near 4 km throughout the peak period with aerosols. The increase of cloud fraction extends to the upper troposphere, near 14 km, corresponding to the increase of ice cloud shown in Figure 5d and 5f. As a result, the deep convection is enhanced associated with more rainfall during peak

time. The similarity of cloud fraction changes between Figure 4b and Figure 4c suggests that ACI dominated the total aerosol effect in this event, which is consistent with the previous discussion.

Figure 5a–5c present the aerosol effects on cloud droplet number concentration (CDNC; shading) and cloud effective radius (contour). With aerosols, CDNC increases dramatically by 5.5 times accompanied by reduced cloud effective radius near 2 km from 00Z on December 14 to 00Z on December 15, which reduces the efficiency of collision-coalescence between cloud droplets into raindrops (Rosenfeld, 2000; Twomey, 1977). This is characterized by less rain water formed in Figure 6c, indicating suppress of the warm rain. Figure 6a shows more cloud water formed at 2–6 km due to higher supersaturation. The consumption of moisture and energy limits the formation of low cloud below. During droplet nucleation due to activating enormous aerosols, there are abundant latent heat release by enhanced condensation below the 0°C isotherm line. This is also reported in Fan et al. (2018) in which the mechanism responsible for convection intensification is latent heat release from cloud water formation with ultrafine aerosols. This is called “warm-phase invigoration” in their study which is different from “cold-phase invigoration” via suppressing the warm rain. Interestingly, unlike their work, the warm rain is still suppressed before 15Z on December 15 (Figure 6c) even though with strong latent heat release through cloud water formation. The rain water is not increased by accretion of added cloud droplets, which implement that the precipitation increase is because of enhancement of cold rain. Both cloud ice number concentration and its effective radius are significantly increased between 6Z and 15Z on 15 December. Moreover, the mass and number of ice crystals including cloud ice, snow, and graupel increase drastically during this period. Note the magnitude of snow and graupel mass is ten times of that of rain water. A distinct latent heat release center appears above 0°C isotherm line, which is even stronger than the condensational heat below. These two peaks in aerosol induced diabatic heating are also discussed in Wang et al. (2014) for oceanic deep convection. However, the peaks at 3 km and 7 km are much higher. This may be because the convection occurs over the land. The latent heat from these two peaks thus will intensify convective strength. These findings suggest the cold-cloud process play a dominant role in the precipitation increase before 15Z on 15 December. To further analyze the source of this latent heat release, following Fan et al. (2018), the latent heat released from condensation, deposition, and freezing during cold and warm cloud processes are diagnosed (Figure 7). The rimming processes are included into the freezing. Cold-phase invigoration by aerosols has been shown in both observational (Andreas et al., 2004) and modeling (Khain et al., 2005; Fan et al., 2007) studies. Particularly, much attention is paid to mixed and cold process in which supercooled droplets are likely to freeze and release latent heat, further enhancing convection (Koren et al., 2008; Rosenfeld et al., 2008; Tao et al., 2007). Interestingly, the latent heat release due to freezing with aerosols is negligible compared with that due to condensation and deposition. The distinct latent heat changes mentioned above in Figure 5g is induced by deposition in cold cloud (Figure 7e). Figure S8 shows the time-height distribution of mass and number concentrations for different hydrometers in control run. Note the magnitude of snow and graupel mass is ten times of that of rain water. There are affluent snow and graupel before 15Z on 15 December located where the distinct changes in depositional heat appears. Smaller cloud effective radius associated with more droplets is produced due to aerosols activation. The subsequent condensational growth lowers the water supersaturation, which is also reported in

Fan et al. (2018). As this occurs, the environment becomes unsaturated to water, resulting in the evaporation of liquid water. This is known as the Bergeron-Findeisen-Wegener theory. With the presence of ice crystals, water vapor deposition is prior to happen on ice surface when the saturation with respect to water is supersaturation with respect to ice. Correspondingly, the ice crystals (i.e. cloud ice, snow, and graupel) increase at the expense of rain water (Figure 6c–e). The latent heat release due to deposition in cold cloud is stronger than that due to condensation in warm cloud though the latter is also very important. After 15Z on December 15, most of the ice crystals fall as precipitation. Compared with depositional heating, the condensational heating plays a dominant role in intensifying convective strength. The rain water increases through accretion of added cloud droplets, leading to precipitation increases. These findings highlight two different processes and mechanisms in the precipitation increase before and after 15Z on December 15. The dominant source for latent heat release is depositional heating in the former case (cold rain enhancement) while condensational heating in the latter (warm rain enhancement). Due to latent heat release with aerosols, the vertical motion is boosted (Figure 5g) which further enhance the supersaturation and associated with latent heat release. Via microphysics–dynamics feedback, the convection is intensified, and precipitation increased. This feedback has been widely discussed in ACI effects on deep convection (Fan et al., 2018; Koren et al., 2015; Tao et al., 2012).

To further delineate the mechanism of this microphysics–dynamics feedback, the moisture budget tool is implemented based on the hourly model output. The atmospheric moisture balance is expressed as follows:

$$\frac{\partial Q}{\partial t} = E - P + MFC \quad (1)$$

where Q is the column-integrated water vapor in the atmosphere, t is time, E is evaporation, P is precipitation, and MFC is the vertically integrated moisture flux convergence.

Evaporation is small in areas of intense precipitation and saturation (Banacos and Schultz, 2005). The column-integrated water vapor changes are small (figure not shown), thus precipitation is balanced by the moisture flux convergence as follows:

$$P \approx MFC \quad (2)$$

MFC can be further divided into two terms as

$$-\frac{1}{g} \int_0^{P_s} \nabla \cdot (q \overline{V}_h) dp = -\frac{1}{g} \int_0^{P_s} q \nabla \cdot \overline{V}_h dp - \frac{1}{g} \int_0^{P_s} \overline{V}_h \cdot \nabla q dp \quad (3)$$

where the first term on the right side is the horizontal moisture convergence (hereafter CON); the second term is the horizontal advection of water vapor (hereafter ADV). Thus the precipitation is balanced by the sum of CON and ADV as

$$P \approx MFC = CON + ADV \quad (4)$$

The spatial distributions of column-integrated MFC (shading) and moisture flux (vector) between CTL and CLEAN on December 15 are displayed in Figure 8a. The MFC pattern is in good agreement with precipitation differences in Figure 3d, suggesting the validity of the derivation of Equation (2). The average MFC change over the analysis region is +8.1 mm, which is comparable to +7.8 mm in precipitation difference. The vertically integrated moisture flux changes in Figure 8a followed

the wind pattern shown in Figure 20. Sd. The moisture flux is enhanced over the analysis region driven by strong convergence, which is consistent with microphysics-dynamics feedback discussed above. These flows converged in the estuary and near the coast with a magnitude of approximately $25 \text{ kg m}^{-1} \text{ s}^{-1}$. The overall pattern of CON is broadly consistent with that of MFC, which indicates that the MFC changes are mainly driven by CON changes (**Error! Reference source not found.a**). The ADV changes contribute about 35% of MFC changes over the analysis region but are much more scattered than CON changes (**Error! Reference source not found.c**). The pattern of differences between CTL and CLEAN resembles that between ARIoff and CLEAN (**Error! Reference source not found.**), which suggest the dominant effect of ACI. The magnitude of changes over the analysis region is smaller in the former case, indicating the compensation effect between ARI and ACI in this case, as noted in section 3.1.

10 These findings reveal the prominent effects of aerosols on rainfall amount over the estuary and near the coast in this extreme rainfall event. The pattern of precipitation and associated cloud-related variables in CTL minus CLEAN (total effects) bears a resemblance to that in ARIoff minus CLEAN (ACI effects), which allows us to ascertain that ACI dominated the total effects. By applying the moisture budget tool, we confirm the microphysical–dynamic feedback of ACI effects on invigorating convection.

15 3.3 Local versus remote aerosol emission effects

A crucial question is the extent to which increased anthropogenic aerosols from either local (i.e., domain 2, which denotes Guangdong province) or remote (i.e., domain 1, which denotes outside Guangdong province) sources result in precipitation changes. Previous studies have reported different roles of local and remote aerosol sources in affecting tropical precipitation (Chou et al., 2005) and monsoons associated with precipitation (Bollasina et al., 2014; Cowan and Cai, 2011) from a climate perspective. However, the differing effects of local and remote aerosols on weather, such as extreme rainfall, are rarely explored. In this section, we examine the roles and relative importance of local and remote aerosols in the precipitation increase in the estuary during this extreme rainfall event.

The differences in time-height cross section of cloud fraction (shading) and $\text{PM}_{2.5}$ concentration (contour) induced by the effects of local and remote emissions are shown in Figure 10a and 10b, respectively. With local emissions, the aerosol concentrations mainly increase within the PBL below 2 km before 12Z on December 15 (Figure 10b). The accumulated aerosols are washed out quickly after the rainfall initiated. By contrast, with remote emissions, a higher aerosol concentration extends to approximately 8 km after 3Z on December 14 (Figure 10a). Two peaks near 0.5 km and 5 km above ground are centered near 10Z and 18Z on December 14, respectively, indicating a strong transportation of aerosols. The earlier peak, near 5 km, is caused by strong wind speed in the free atmosphere compared with that within the PBL. Moreover, the aerosol concentrations last longer before decreasing dramatically until the peak rainfall starts at 07Z on December 15, because aerosols are transported continuously from the remote area. The cloud fraction reduction is coherent with aerosol concentration peaks, indicating that increased aerosols lead small cloud droplets to evaporate. Moreover, more deep cloud formation consuming moisture and energy. Comparing patterns of cloud fraction changes between Figure 10a and 10b and Figure 4b indicate the

dominant effects of aerosols from remote areas. The CDNC (shading) increases in both D1 and D2 runs compared with the CLEAN run before the rainfall peak (Figure 11a and 11b). However, the discernible cloud effective radius (contours) decrease appears only in the D1 run and is attributed to a stronger CDNC increase. Correspondingly, the CINC and ice cloud effective radius show more remarkable increases in the D1 run during the rainfall peak time (Figure 11c and 11d). The associated latent heat and vertical velocity are much stronger in the D1 run compared with the D2 run (Figure 11e and 11f). Interestingly, most of latent heat release with local emissions are happened below 0°C isotherm line. Figure 12 shows the changes in mass and number of different hydrometeors with remote aerosols emissions. There are plenty of snow and graupel formation at the expense of rain water when precipitation increase before 15Z on 15 December, indicating intensified cold rain process. The corresponding latent heat release is dominated by deposition in cold cloud. By contrast, after 15Z on 15 December 15, rain water increases significantly during precipitation enhancement, representing stronger warm rain process. The associated latent heat release is due to condensation heating in warm cloud concentrated below 0°C isotherm line. The patterns of changes in hydrometeors and latent heat in D1 assembles that in CTL run, which further confirm the dominant role of remote aerosols emissions. The distribution of time-height changes in hydrometeors and latent heat between D2 and CLEAN run are shown in Figure S9 and Figure S10, respectively. As aerosols from local emissions are washed out dramatically once the rain initiated, much less cloud water formed than that in D1 run. Thus, the supersaturation is lowered as strongly as that in D1 simulation. More rain water is formed by accretion of cloud droplets which indicate that intensified warm rain is the only reason for precipitation increase with local aerosol emissions. As a result, the average precipitation increase over the analysis region on December 15 is 7.3 mm with remote aerosol emissions, much greater than that with local aerosol emissions (3.1 mm, Figure 14c and 14d). These findings suggest that both the effects of local and, to a much greater extent, remote aerosol emissions contribute to precipitation increases over the analysis region.

3.4 Tenfold anthropogenic emissions and chemical ICs and BCs

An optimal aerosol loading should exist in which the convection is the most vigorous (Rosenfeld et al., 2008). For aerosol concentrations below the optimum, the convection is invigorated by smaller droplets; thus, stronger updraft releases larger latent release (Dagan et al., 2015b). By contrast, suppression effects dominate above the optimum (Small et al., 2009). The optimum value is determined by environmental conditions (e.g., relative humidity, see Dagan et al., 2015a). In this section, a tenfold aerosol emission simulation (10×) is conducted to examine the sensitivity of precipitation and associated cloud properties to aerosol concentrations.

The PM_{2.5} concentrations (contours) in 10× increased significantly to approximately ten times that in CTL, indicating a linear relationship from emissions to aerosol concentration (Figure 15). The associated boundary layer cloud formation (shading) is further suppressed below 2 km, which is consistent with the result in Figure 4b. The change patterns in cloud fraction and aerosol concentration in Figure 15. D are similar to that in Figure 4b, but Figure 15 shows a much greater magnitude. The CDNC (shading) increase and cloud effective radius (contours) reduction in Figure 16a are also more pronounced than those

in Figure 5a. CDNC noticeably decreases below 1.5 km but increases substantially from 1.5 km to 4 km before 04Z on December 14, associating with smaller radius. Smaller cloud droplet tends to evaporate. In addition, more cloud droplets are produced due to higher supersaturation upward. The consumption of water and energy leads to further reduction of low cloud (Figure 17a). The involved latent heat and vertical velocity during the rainfall peak time from 8Z on December 15 to 10Z on December 16 in Figure 16c exhibit a stronger increase associated with a higher altitude above the freezing level than that in Figure 5c. Besides, a distinct weaker latent heat release associated with negative vertical velocity anomaly appear below freezing level between 10Z and 22Z on 15 December. This indicate a more important role of cold related processes in latent heat release. The ice crystals also increase drastically with bigger radius. Figure 17 shows the changes in mass and number concentrations of different hydrometeors in 10 \times simulation. Compared with CTL run, the snow and graupel are also increased with a stronger magnitude, particularly before 15Z on 15 December, indicating enhanced cold rain. However, rain water show decrease during all the time instead of increase after 15Z when precipitation increase. This means the warm rain is suppressed much stronger in 10 \times simulation. As with ten times of aerosols emissions, the aerosols lower the supersaturation much stronger by activation to form much smaller cloud droplets. The rain water evaporates rather than increase by accretion of additional cloud droplet, associating with strong condensational cooling in warm cloud (Figure 18a). Precipitation on December 15 is suppressed over the upstream region up to 39.6 mm in the northwest of Guangdong province but substantially enhanced up to 59.7 mm over the downstream region near the coastal region (Figure 19b). A similar finding is reported by Zhong et al. (2015). The delay of early rain in the upstream area results in more rainfall and stronger rain intensity within the downstream area and a more narrowed region compared with the red box in Figure 3b. The average precipitation in Guangdong province on December 15 decrease by 1.0 mm in 10 \times , whereas it increases by 1.4 mm in CTL. Tenfold aerosol emissions produce a more polluted environment, with PM_{2.5} concentrations of approximately 300 $\mu\text{g m}^{-3}$. Although abundant moisture is transported from the Bay of Bengal and the South China Sea (Figure 1b), the aerosol loading may still have surpassed the optimal value for cloud invigoration and thus suppressed precipitation over Guangdong province. Moreover, aside from suppressing the rainfall amount, excessive aerosols also have the potential to redistribute precipitation and increase its range in spatial distribution.

25 4 Summary and discussion

In this study, we find that aerosols significantly affect local extreme weather (i.e., torrential rainfall), invigorating deep convection, via ACI effects. Deep convection invigoration by aerosols has been discussed in both observation (Andreae et al., 2004; Koren et al., 2004) and model simulations (Khain et al., 2005; Storer et al., 2013). Most of these studies are focused on mixed and cold processes. Increasing aerosols can suppress warm rain because of smaller cloud droplets. These smaller cloud droplets are likely lifted upward to freeze. The latent heat due to freezing will further enhance convection (Rosenfeld et al., 2008). This is referred to as cold-phase invigoration. A recent interesting study conducted by Fan et al. (2018) found that additional nucleation of cloud droplet can release abundant condensational heat below freezing level. More cloud water will

form via condensation on the additional cloud droplets. This process will increase both warm rain and supercooled cloud water. Furthermore, the ice-related processes are enhanced with latent heat release, further intensifying the convection. In their study, the source of latent heat is dominated by condensational heating, accompanied by enhanced warm rain. In contrast to cold-phase invigoration, the concept of warm-phased invigoration is proposed in this work.

5 With aerosols, the precipitation is increased between 03Z on December 15 to 10Z on December 16. CDNC increases remarkably, reducing the size of cloud droplets, which lowers supersaturation significantly through condensation enhancement. Additional cloud water formed with intensified condensational heating, leading to enhanced convection and increased precipitation. However, rain water decreased substantially before 15Z on 15 December, indicating suppressed warm rain, which is different to Fan et al. (2018). The source of latent heat release is dominated by deposition in cold cloud associate with
10 increase of snow and graupel, representing cold rain enhancement. There are abundant ice crystals including snow and graupel at 4–6 km from 00Z to 15Z on 15 December. As aerosols activation decreases the supersaturation, with presence of ice crystals, water vapor deposition on ice is more likely to happen because the saturation with respect to water is supersaturation with respect to ice. The environment become unsaturated to water when this situation occurs, resulting in evaporation of rain water. This process is known as the Bergeron-Findeisen-Wegener theory. As a result, the mass and number of ice crystals increase
15 drastically at the expense of rain water, suggesting a dominant role of cold rain before 15Z on 15 December. Most of snow and graupel fall as precipitation when the peak rainfall occurs after 15Z. By contrast, the warm rain is enhanced characterized by increase of rain water associating with condensational heating in warm cloud via accretion of cloud droplet, which is consistent with Fan et al. (2018). The enhanced latent heat boosts the vertical motion, leading to higher supersaturation accompanied by stronger latent heat release. This feedback between microphysical and dynamic processes results in more
20 rainfall (Tao et al., 2007) up to 33.7 mm in our simulation. On average, ACI enhance precipitation over the analysis region. Conversely, ARI partially compensate for the precipitation increase by 14%. The analysis of the moisture budget suggests that the precipitation increase is manifested by strengthening the column-integrated MFC. Further decomposition of MFC suggest the importance of horizontal moisture convergence. Our finding confirms that microphysical–dynamic feedback is at the core of the effects of ACI on convection invigoration.

25 An interesting question is why the precipitation increases induced by ACI appear on land near the Pearl River estuary and the coast. Khain et al. (2008) found that aerosols generally suppress cloud formation in relatively dry conditions, whereas they invigorate convection in moist environments. Fan et al. (2009) suggested that wind shear may take a dominant role in regulating the effects of aerosol on deep convection. Increased aerosols suppress (invigorate) convection under strong (weak) wind shear. These findings highlight the crucial roles of humidity and wind shear in modulating the cloud invigoration effects induced by
30 aerosols. Strong wind shear enhances the entrainment of dry air into clouds and transports cloud liquid to unsaturated regions; this leads to greater evaporation and sublimation of cloud particles. These processes are associated with cooling, downdrafts, and convergence, especially at high aerosol concentrations (Khain, 2009; Lee et al., 2008). The convergence thus fosters secondary cloud formation and contributes to an increase in precipitation. However, Fan et al. (2009) stressed that the net latent heat release, as an energy source for convection, is greater under weak wind shear than under strong wind shear. Aerosols

enhance convection under weak wind shear until an optimal aerosol concentration is reached at which the net latent heat release equilibrates. This mechanism may only be applicable to isolated storms rather than to cloud systems. Note that the previous studies have used different wind components (zonal component, meridional component, or total wind) at different heights with different thresholds (e.g., upper limits vary from 10 m s^{-1} to 20 m s^{-1}). These different standards may only be suitable for specific environmental conditions, because previous studies have been based on limited cases. In our work, the wind shear is estimated as the difference between the maximum and minimum total wind speeds at 0–10 km. The spatial distribution of wind shear (first row) and column-integrated water vapor (second row) are presented in Figure 20. The wind shear increases with the southeast–northwest tilt ranging from 35 m s^{-1} to 80 m s^{-1} (Figure 20a and 20b). Our definition of wind shear is different from other studies (e.g., Lee et al. 2008; Fan et al. 2009; Li et al. 2011; Guo et al., 2016a), with a higher altitude. We chose 10 km because the latent heat release, which is a key factor determining convection intensity and partly depends on wind shear, extends up to approximately 10 km (Figure 5g). Although the wind shear in our work is stronger than that in other studies with magnitudes lower than 10 m s^{-1} , the aerosol invigoration effect appears over the region with relatively weak wind shear and high humidity on the land along the coast, as presented in Figure 20. This invigoration effect under weak wind shear for cloud systems is described in a recent work (Li et al., 2011), whereas it is to some extent contradicted by the results of Lee et al. (2008). Conversely, precipitation was suppressed to the northwest of Guangdong, with relatively strong wind shear and low humidity, as shown in Figure 20b and 20d. The gradients of wind shear and humidity increase between the southeast and northwest of domain 2 on December 15 when peak rainfall occurred. The results confirm that the effect of aerosols on precipitation is related to relative humidity and wind shear. However, this relationship remains dependent on the situation and may be affected by other meteorological variables, such as convective available potential energy (Khain et al., 2005), cloud phase (Lin et al., 2006), and cloud type (Koren et al., 2008). The relative importance of different meteorological variables in regulating the aerosol-induced precipitation effect requires both long-term observation and model sensitivity tests to provide a more comprehensive picture.

Aerosol emissions were separated into those from Guangdong Province and those from elsewhere, named experiments D2 and D1, respectively, to represent the effects of aerosol concentrations from local and remote emissions on this extreme rainfall event. The surface aerosol concentrations accumulate slowly from local emissions if the rainfall system comes with strong northerlies. Instead, aerosols, transport from remote areas persistently, extend to higher altitudes, up to 8 km. The aerosol concentrations thus are maintained at a relatively high level in the D1 and invigorated convection. The resemblance of changes in different hydrometeors and latent heat between D1 and CTL further suggest the dominant role of remote aerosols in the convection invigoration. Interestingly, with local emissions, the precipitation enhancement is mainly through intensified warm rain only. This is because much less aerosols stay in the atmosphere with only local aerosols emissions once the rainfall initiated. The effect of nucleated cloud droplets on reducing supersaturation is much weaker than that with remote aerosol emissions. Thus, the rain water is increased by accretion of cloud droplets, enhancing the warm rain. The precipitation averaged over the analysis region on December 15 increased by 7.3 mm from the effects of remote aerosol emissions but only 3.1 mm from local aerosol emissions. These results suggest that the effects of remote aerosol emissions play a dominant role in the

intensification of precipitation in the estuary, which implies the potential influence of remote aerosol emissions on extreme synoptic weather events. However, this crucial issue remains insufficiently explored.

Previous studies have suggested an optimal aerosol loading in which condensational heating and evaporative cooling are balanced, leading to the most vigorous convection (Fan et al., 2007, 2009; Rosenfeld et al., 2008; Wang, 2005). A tenfold emission experiment showed a similar pattern with CTL but with a much stronger signal. Further analysis of hydrometeors and latent heat reveal that the main reason for precipitation increase is via intensified cold rain. The warm rain is suppressed almost all the time because the reduction of supersaturation due to cloud droplet nucleation is much stronger than that in CTL run. As a result, only the ice-related processes are intensified based on the Bergeron-Findeisen-Wegener theory. Instead, the increase of rain water by accretion of droplets is suppressed. Excessive aerosols lead to more precipitation increases, up to 59.7 mm, which is much larger than the 33.7 mm from CTL. However, the precipitation increase is limited to a more narrowed region along the coast in the downwind area; this may be related to the adequate supply of water vapor from onshore wind, as shown in Figure 20d. The average precipitation over Guangdong province decreased by 1.0 mm in 10^x but increased by 1.4 mm in CTL. These results indicate that aerosol concentrations in 10^x exceed the optimal aerosol loading for convection invigoration and instead suppress the rainfall amount. The retribution for spatial distribution of precipitation with a sharper contrast implies that air pollution may increase the possibility of both flood and drought.

The mechanism of precipitation over another region, in 24°–25°N, 110°–112°E, is also investigated. Figure S11 shows the distribution of time-height mass and number concentrations of different hydrometeors averaged over this region from CTL run. There are lots of ice crystals with cloud ice extending up to 16 km, indicating strong deep convection, which is consistent with low cloud top temperature in Figure S1b. With aerosols, more cloud droplets nucleated on which water can condensate. Additional cloud water is subsequently formed near to 4 km (Figure S12a), accompanied by reduced supersaturation. The reduction of rain water and ice crystals (particularly in graupel) suggest that both the warm rain and cold rain are suppressed. Less latent heat is released dominated by condensation in warm cloud and deposition in cold cloud. There could be two reasons for this. The first one is that the mass of water vapor is small over this region in the northwest corner of the domain, so that not enough water supply for convection invigoration effect with aerosols. The other one is related to the very strong wind shear over this region with maximum value up to 80 m s⁻¹. This condition is unfavored for latent heat to accumulate, which is key factor to convection strength (Fan et al., 2009). Thus, the precipitation is suppressed over this region with aerosols. With ten times of aerosol emissions, the mass and number of rain water and ice crystals are further reduced, accompanied by weaker latent heat release. As a result, the precipitation is further suppressed (Figure 19b).

We note that uncertainties exist in aerosol emission and the representation of ACI. Although ice nucleation may have little effect on the spatial distribution and temporal evolution of surface precipitation (Deng et al., 2018), this factor is not yet considered in the WRF-Chem model. This may explain negligible differences in results between simulations with and without dust and sea salt emissions. Additionally, dust sources are far from our analysis region and the prevailing wind is northerly; these produce low dust and sea salt concentrations, respectively. It is noteworthy that we assume the ARI and ACI effects are linear additive as previous studies (Fan et al., 2015; Zhong et al., 2015), so that the ACI effect is derived by subtracting ARI

from total aerosol effects. We cannot check the nonlinearity between ARI and ACI effects because it is not easy to turn off ACI effect. The problem is how to set the background concentration of cloud droplet number while keep the ARI as same in control run. This means that we could only prescribe the cloud droplet number concentration rather than adjust the emission or aerosol concentration. However, the ACI effect is very sensitive to the number we set (Gustafson et al., 2007).

5 Although our findings are limited to a case study, this case is, nevertheless, representative of the remarkable aerosol effect on an extreme rainfall event through ACI. This finding provides more evidence of the importance of considering aerosols in extreme weather (i.e., torrential rainfall) forecasting. More interestingly, aerosols from remote emission sources exhibited the potential to modify extreme weather through transboundary air pollution. This case clearly demonstrates the complicated feedback between the dynamic and microphysical processes induced by aerosols. Aerosols substantially redistributed the rainfall amount, a finding with crucial implications for the availability and usability of water resources in different regions of the world (Li et al., 2011). High aerosol concentrations may intensify both flood and drought by invigorating convection.

Acknowledgment. This work was jointly supported by the Early Career Scheme of Research Grants Council of Hong Kong (grant CUHK24301415), the National Key Basic Research Program of China (grant 2015CB954103), the Ministry of Science and Technology of China (grant 2017YFC1501401), the Improvement on Competitiveness in Hiring New Faculties Fund (2013/2014) of The Chinese University of Hong Kong (CUHK, grant 4930059), and the Vice-Chancellor's Discretionary Fund of the Chinese University of Hong Kong (grant 4930744). The appointment of NCL at the CUHK is supported by the AXA Research Fund. Model simulations were conducted on computer clusters at Geophysical Fluid Dynamics Laboratory (GFDL). Larry Horowitz and Maofeng Liu provided helpful comments. We acknowledge the Global Scholarship Program for Research Excellence 2017–18 at the CUHK for supporting Zhen Liu's exchange visit to Princeton University. Chun Zhao is supported by the Thousand Talents Plan for Young Professionals, the Fundamental Research Funds for the Central Universities, and the National Natural Science Foundation of China (grant 41775146).

Author contribution

S.H.L. Yim planned, supervised and sought funding for this study. Z. Liu conducted the study and drafted the manuscript with SH.L. Yim. Other co-authors provided comments on the results and the manuscript.

References

- Altaratz, O., Koren, I., Remer, L. A. and Hirsch, E.: Review: Cloud invigoration by aerosols-Coupling between microphysics and dynamics, *Atmos. Res.*, 140–141, 38–60, doi:10.1016/j.atmosres.2014.01.009, 2014.
- Andreae, M. O., Rosenfeld, D., Artaxo, P., Costa, A. A., Frank, G. P., Longo, K. M. and Silva-Dias, M. A. F.: Smoking rain clouds over the Amazon, *Science*, 303(5662), 1337–1342, doi:10.1126/science.1092779, 2004.

- Banacos, P. C. and Schultz, D. M.: The use of moisture flux convergence in forecasting convective initiation: historical and operational perspectives, *Weather Forecast.*, 20(3), 351–366, doi:10.1175/WAF858.1, 2005.
- Bell, T. L., Rosenfeld, D., Kim, K. M., Yoo, J. M., Lee, M. I. and Hahnenberger, M.: Midweek increase in U.S. summer rain and storm heights suggests air pollution invigorates rainstorms, *J. Geophys. Res. Atmos.*, 113(2),
5 doi:10.1029/2007JD008623, 2008.
- Binkowski, F. S. and Shankar, U.: The regional particulate matter model: 1. Model description and preliminary results, *J. Geophys. Res.*, 100(D12), 26191, doi:10.1029/95JD02093, 1995.
- Bollasina, M. A., Ming, Y. and Ramaswamy, V.: Anthropogenic aerosols and the weakening of the South Asian summer monsoon, *Science*, 334(6055), 502–505, doi:10.1126/science.1204994, 2011.
- 10 Bollasina, M. A., Ming, Y., Ramaswamy, V., Schwarzkopf, M. D. and Naik, V.: Contribution of local and remote anthropogenic aerosols to the twentieth century weakening of the South Asian Monsoon, *Geophys. Res. Lett.*, 41(2), 680–687, doi:10.1002/2013GL058183, 2014.
- Chang, C.-P., Z. Wang, and H. Hendon: The Asian winter monsoon, *The Asian Monsoon*, B. Wang, Ed., Springer, 89–127, 2006.
- 15 Chang, W., Zhan, J., Zhang, Y., Li, Z., Xing, J. and Li, J.: Emission-driven changes in anthropogenic aerosol concentrations in China during 1970–2010 and its implications for PM_{2.5} control policy, *Atmos. Res.*, doi:10.1016/j.atmosres.2018.05.008, 2018.
- Chapman, E. G., Gustafson, W. I., Easter, R. C., Barnard, J. C., Ghan, S. J., Pekour, M. S. and Fast, J. D.: Coupling aerosol-cloud-radiative processes in the WRF-Chem model: Investigating the radiative impact of elevated point sources, *Atmos. Chem. Phys.*, 9(3), 945–964, doi:10.5194/acp-9-945-2009, 2009.
- 20 Chen, F. and Dudhia, J.: Coupling an advanced land surface–hydrology model with the Penn State–NCAR MM5 modeling system. Part I: Model implementation and sensitivity, *Mon. Weather Rev.*, 129(4), 569–585, doi:10.1175/1520-0493(2001)129<0569:CAALSH>2.0.CO;2, 2001.
- Chen, T., Guo, J., Li, Z., Zhao, C., Liu, H., Cribb, M., Wang, F. and He, J.: A CloudSat perspective on the cloud climatology and its association with aerosol perturbations in the vertical over Eastern China, *J. Atmos. Sci.*, 73(9), 3599–3616,
25 doi:10.1175/JAS-D-15-0309.1, 2016.
- Chen X. C., Jahn H. J., Engling G., Ward T. J., Kraemer A., Ho K. F., Yim S. H. L., Chan C. Y.: Chemical characterization and sources of personal exposure to fine particulate matter (PM_{2.5}) in the megacity of Guangzhou, China., *Environ. Pollut.*, 231, 871–881, 2017.
- 30 Chou, C., Neelin, J. D., Lohmann, U. and Feichter, J.: Local and remote impacts of aerosol climate forcing on tropical precipitation, *J. Clim.*, 18(22), 4621–4636, doi:10.1175/JCLI3554.1, 2005.
- Cohen A J, Brauer M, Burnett R, et al.: Estimates and 25-year trends of the global burden of disease attributable to ambient air pollution: an analysis of data from the Global Burden of Diseases Study, *The Lancet*, 2017, 389 (10082), 1907-1918, 2015.

- Cowan, T. and Cai, W.: The impact of Asian and non-Asian anthropogenic aerosols on 20th century Asian summer monsoon, *Geophys. Res. Lett.*, 38(11), doi:10.1029/2011GL047268, 2011.
- Cui, Z. Q., Carslaw, K. S., Yin, Y. and Davies, S.: A numerical study of aerosol effects on the dynamics and microphysics of a deep convective cloud in a continental environment, *J. Geophys. Res.*, 111(D5), D05201, doi:10.1029/2005JD005981, 2006.
- Dagan, G., Koren, I. and Altaratz, O.: Aerosol effects on the timing of warm rain processes, *Geophys. Res. Lett.*, 42(11), 4590–4598, doi:10.1002/2015GL063839, 2015a.
- Dagan, G., Koren, I. and Altaratz, O.: Competition between core and periphery-based processes in warm convective clouds – from invigoration to suppression, *Atmos. Chem. Phys.*, 15(5), 2749–2760, doi:10.5194/acp-15-2749-2015, 2015b.
- Dee, D. P., Uppala, S. M., Simmons, A. J., Berrisford, P., Poli, P., Kobayashi, S., ... Vitart, F.: The ERA-Interim reanalysis: Configuration and performance of the data assimilation system. *Q. J. Royal Meteorol. Soc.*, 137(656), 553–597. <https://doi.org/10.1002/qj.828>, 2011.
- Deng, W. J., Wu, N. G., Lin, L. X., and Zhang, H., L.: Causal analysis of an unusual continuous torrential rainfall event in Guangdong in the winter of 2013, *Meteor. Sci. Technol.*, 43(2), 276–282, doi:10.19517/j.1671-6345.2015.02.019, 2015.
- Deng, X., Xue, H. and Meng, Z.: The effect of ice nuclei on a deep convective cloud in South China, *Atmos. Res.*, 206, 1–12, doi:10.1016/j.atmosres.2018.02.013, 2018.
- Ding, A., Wang, T., Xue, L., Gao, J., Stohl, A., Lei, H., Jin, D., Ren, Y., Wang, X., Wei, X., Qi, Y., Liu, J. and Zhang, X.: Transport of north China air pollution by midlatitude cyclones: Case study of aircraft measurements in summer 2007, *J. Geophys. Res. Atmos.*, 114(8), doi:10.1029/2008JD011023, 2009.
- Ding, A. J., Fu, C. B., Yang, X. Q., Sun, J. N., Petäjä, T., Kerminen, V. M., Wang, T., Xie, Y., Herrmann, E., Zheng, L. F., Nie, W., Liu, Q., Wei, X. L. and Kulmala, M.: Intense atmospheric pollution modifies weather: A case of mixed biomass burning with fossil fuel combustion pollution in eastern China, *Atmos. Chem. Phys.*, 13(20), 10545–10554, doi:10.5194/acp-13-10545-2013, 2013.
- Dutot, A. L., Rynkiewicz, J., Steiner, F. E. and Rude, J.: A 24-h forecast of ozone peaks and exceedance levels using neural classifiers and weather predictions, *Environ. Model. Softw.*, 22(9), 1261–1269, doi:10.1016/j.envsoft.2006.08.002, 2007.
- Easter, R. C., Ghan, S. J., Zhang, Y., Saylor, R. D., Chapman, E. G., Laulainen, N. S., Abdul-Razzak, H., Leung, L. R., Bian, X. and Zaveri, R. A.: MIRAGE: Model description and evaluation of aerosols and trace gases, *J. Geophys. Res. D Atmos.*, 109(20), doi:10.1029/2004JD004571, 2004.
- Emmons, L. K., Walters, S., Hess, P. G., Lamarque, J.-F., Pfister, G. G., Fillmore, D., Granier, C., Guenther, A., Kinnison, D., Laepfle, T., Orlando, J., Tie, X., Tyndall, G., Wiedinmyer, C., Baughcum, S. L. and Kloster, S.: Description and evaluation of the Model for Ozone and Related chemical Tracers, version 4 (MOZART-4), *Geosci. Model Dev.*, 3(1), 43–67, doi:10.5194/gmd-3-43-2010, 2010.
- Fan, J., Zhang, R., Li, G. and Tao, W. K.: Effects of aerosols and relative humidity on cumulus clouds, *J. Geophys. Res. Atmos.*, 112(14), doi:10.1029/2006JD008136, 2007.

- Fan, J., Zhang, R., Tao, W.-K. and Mohr, K. I.: Effects of aerosol optical properties on deep convective clouds and radiative forcing, *J. Geophys. Res.*, 113(D8), D08209, doi:10.1029/2007JD009257, 2008.
- Fan, J., Yuan, T., Comstock, J. M., Ghan, S., Khain, A., Leung, L. R., Li, Z., Martins, V. J. and Ovchinnikov, M.: Dominant role by vertical wind shear in regulating aerosol effects on deep convective clouds, *J. Geophys. Res. Atmos.*, 114(22),
5 doi:10.1029/2009JD012352, 2009.
- Fan, J., Rosenfeld, D., Ding, Y., Leung, L. R. and Li, Z.: Potential aerosol indirect effects on atmospheric circulation and radiative forcing through deep convection, *Geophys. Res. Lett.*, 39(9), doi:10.1029/2012GL051851, 2012.
- Fan, J., Leung, L. R., Rosenfeld, D., Chen, Q., Li, Z., Zhang, J. and Yan, H.: Microphysical effects determine macrophysical response for aerosol impacts on deep convective clouds, *Proc. Natl. Acad. Sci.*, 110(48), E4581–E4590,
10 doi:10.1073/pnas.1316830110, 2013.
- Fan, J., Rosenfeld, D., Yang, Y., Zhao, C., Leung, L. R. and Li, Z.: Substantial contribution of anthropogenic air pollution to catastrophic floods in Southwest China, *Geophys. Res. Lett.*, n/a-n/a, doi:10.1002/2015GL064479, 2015.
- Fan, J., Rosenfeld, D., Zhang, Y., Giangrande, S. E., Li, Z., Machado, L. A. T., Martin, S. T., Yang, Y., Wang, J., Artaxo, P.,
15 Barbosa, H. M. J., Braga, R. C., Comstock, J. M., Feng, Z., Gao, W., Gomes, H. B., Mei, F., Pöhlker, C., Pöhlker, M. L.,
Pöschl, U. and De Souza, R. A. F.: Substantial convection and precipitation enhancements by ultrafine aerosol particles, *Science* (80-.), doi:10.1126/science.aan8461, 2018.
- Fast, J. D., Gustafson, W. I., Easter, R. C., Zaveri, R. A., Barnard, J. C., Chapman, E. G., Grell, G. A. and Peckham, S. E.: Evolution of ozone, particulates, and aerosol direct radiative forcing in the vicinity of Houston using a fully coupled meteorology-chemistry-aerosol model, *J. Geophys. Res. Atmos.*, 111(21), 1–29, doi:10.1029/2005JD006721, 2006.
- 20 Fu, G., Yu, J., Yu, X., Ouyang, R., Zhang, Y., Wang, P., Liu, W. and Min, L.: Temporal variation of extreme rainfall events in China, 1961-2009, *J. Hydrol.*, 487, 48–59, doi:10.1016/j.jhydrol.2013.02.021, 2013.
- Graf, H. F.: The complex interaction of aerosols and clouds, *Science*, 303(5662), 1309–1311, doi:10.1126/science.1094411, 2004.
- Grell, G., Freitas, S. R., Stuefer, M. and Fast, J.: Inclusion of biomass burning in WRF-Chem: Impact of wildfires on weather
25 forecasts, *Atmos. Chem. Phys.*, 11(11), 5289–5303, doi:10.5194/acp-11-5289-2011, 2011.
- Grell, G. A., Peckham, S. E., Schmitz, R., McKeen, S. A., Frost, G., Skamarock, W. C. and Eder, B.: Fully coupled “online” chemistry within the WRF model, *Atmos. Environ.*, 39(37), 6957–6975, doi:10.1016/j.atmosenv.2005.04.027, 2005.
- Gu, Y. and Yim, S. H. L.: The air quality and health impacts of domestic trans-boundary pollution in various regions of China, *Environ. Int.*, 97, 117–124, doi:10.1016/j.envint.2016.08.004, 2016.
- 30 Gunn, R. and Phillips, B. B.: An experimental investigation of the effect of air pollution on the Initiation of rain, *J. Meteorol.*, 14, 272–279, 1957.
- Guo, J., Deng, M., Lee, S. S., Wang, F., Li, Z., Zhai, P., Liu, H., Lv, W., Yao, W. and Li, X.: Delaying precipitation and lightning by air pollution over the pearl river delta. Part I: Observational analyses, *J. Geophys. Res.*, 121(11), 6472–6488, doi:10.1002/2015JD023257, 2016a.

- Guo, L., Turner, A. G. and Highwood, E. J.: Local and remote impacts of aerosol species on Indian summer monsoon rainfall in a GCM, *J. Clim.*, 29(19), 6937–6955, doi:10.1175/JCLI-D-15-0728.1, 2016b.
- Guo J., Lou M., Miao Y., Wang Y., Zeng Z., Liu H., He J., Xu H., Wang F., Min M., and Zhai P.: Trans-Pacific transport of dust aerosol originated from East Asia: Insights gained from multiple observations and modeling, *Environ. Poll.*, 230, 1030–1039, 10.1016/j.envpol.2017.07.062, 2017.
- Gustafson, W. I., Chapman, E. G., Ghan, S. J., Easter, R. C. and Fast, J. D.: Impact on modeled cloud characteristics due to simplified treatment of uniform cloud condensation nuclei during NEAQS 2004, *Geophys. Res. Lett.*, 34(19), L19809, doi:10.1029/2007GL030021, 2007.
- He, K., Huo, H. and Zhang, Q.: Urban air pollution in China: Current status, characteristics, and progress, *Annu. Rev. Energy Environ.*, 27(1), 397–431, doi:10.1146/annurev.energy.27.1.22001.083421, 2002.
- Hong, S.-Y., Noh, Y. and Dudhia, J.: A new vertical diffusion package with an explicit treatment of entrainment processes., *Mon. Weather Rev.*, 134(9), 2318–2341, doi:10.1175/MWR3199.1, 2006.
- Hu, Z., Zhao, C., Huang, J., Leung, L. R., Qian, Y., Yu, H., Huang, L. and Kalashnikova, O. V.: Trans-Pacific transport and evolution of aerosols: Evaluation of quasi-global WRF-Chem simulation with multiple observations, *Geosci. Model Dev.*, 9(5), 1725–1746, doi:10.5194/gmd-9-1725-2016, 2016.
- Iacono, M. J., Delamere, J. S., Mlawer, E. J., Shephard, M. W., Clough, S. A. and Collins, W. D.: Radiative forcing by long-lived greenhouse gases: Calculations with the AER radiative transfer models, , 113, 2–9, doi:10.1029/2008JD009944, 2008.
- Iltoviz, E., Khain, A. P., Benmoshe, N., Phillips, V. T. J. and Ryzhkov, A. V.: Effect of Aerosols on Freezing Drops, Hail, and Precipitation in a Midlatitude Storm, *J. Atmos. Sci.*, doi:10.1175/JAS-D-14-0155.1, 2016.
- IPCC, 2013: Climate Change 2013: The physical science basis. Contribution of Working Group I to the fifth assessment report of the Intergovernmental Panel on Climate Change [Stocker, T.F., Qin, G.-K., Plattner, M., Tignor, S.K., Allen, J., Boschung, A., Nauels, Y., Xia, V., Bex, and P.M. Midgley (eds.)]. Cambridge University Press, Cambridge, United Kingdom and New York, NY, USA, 1535 pp, doi:10.1017/CBO9781107415324.
- Janssens-Maenhout, G., Crippa, M., Guizzardi, D., Dentener, F., Muntean, M., Pouliot, G., Keating, T., Zhang, Q., Kurokawa, J., Wankmüller, R., Denier Van Der Gon, H., Kuenen, J. J. P., Klimont, Z., Frost, G., Darras, S., Koffi, B. and Li, M.: HTAP-v2.2: A mosaic of regional and global emission grid maps for 2008 and 2010 to study hemispheric transport of air pollution, *Atmos. Chem. Phys.*, 15(19), 11411–11432, doi:10.5194/acp-15-11411-2015, 2015.
- Jiang, J. H., Su, H., Huang, L., Wang, Y., Massie, S., Zhao, B., Omar, A. and Wang, Z.: Contrasting effects on deep convective clouds by different types of aerosols, *Nat. Commun.*, doi:10.1038/s41467-018-06280-4, 2018.
- Jiang, Q., Li, W., Wen, J., Qiu, C., Sun, W., Fang, Q., Xu, M. and Tan, J.: Accuracy evaluation of two high-resolution satellite-based rainfall products: TRMM 3B42V7 and CMORPH in Shanghai, *Water (Switzerland)*, 10(1), doi:10.3390/w10010040, 2018.
- Jin, Q., Yang, Z. L. and Wei, J.: Seasonal responses of Indian summer monsoon to dust aerosols in the middle East, India, and

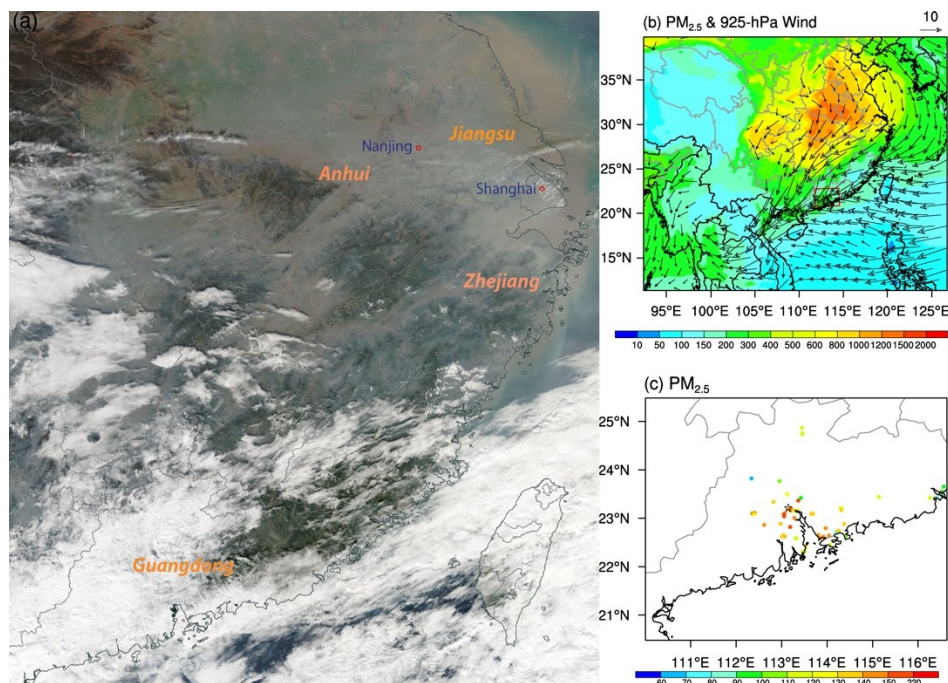
- China, *J. Clim.*, 29(17), 6329–6349, doi:10.1175/JCLI-D-15-0622.1, 2016.
- Joyce, R. J., Janowiak, J. E., Arkin, P. A. and Xie, P.: CMORPH: A method that produces global precipitation estimates from passive microwave and infrared data at high spatial and temporal resolution, *J. Hydrometeorol.*, 5(3), 487–503, doi:10.1175/1525-7541(2004)005<0487:CAMTPG>2.0.CO;2, 2004.
- 5 Kain, J. S. and J. M. Fritsch: A one-dimensional entraining/detraining plume model and its application in convective parameterization, *J. Atmos. Sci.*, 47, 2784–2802, doi.org/10.1175/1520-0469(1990)047<2784:AODEPM>2.0.CO;2, 1990.
- Kaufman, Y. J. and Koren, I.: Smoke and pollution aerosol effect on cloud cover, *Science*, 313(5787), 655–658, doi:10.1126/science.1126232, 2006.
- 10 Khain, A., Rosenfeld, D. and Pokrovsky, A.: Aerosol impact on the dynamics and microphysics of deep convective clouds, *Q. J. R. Meteorol. Soc.*, 131(611), 2639–2663, doi:10.1256/qj.04.62, 2005.
- Khain, A. P.: Notes on state-of-the-art investigations of aerosol effects on precipitation: A critical review, *Environ. Res. Lett.*, 4(1), doi:10.1088/1748-9326/4/1/015004, 2009.
- Khain, A. P., BenMoshe, N. and Pokrovsky, A.: Factors determining the impact of aerosols on surface precipitation from
15 clouds: An attempt at classification, *J. Atmos. Sci.*, 65(6), 1721–1748, doi:10.1175/2007JAS2515.1, 2008.
- Koren, I., Kaufman, Y. J., Remer, L. A. and Martins, J. V.: Measurement of the effect of amazon smoke on inhibition of cloud formation, *Science*, 303(5662), 1342–1345, doi:10.1126/science.1089424, 2004.
- Koren, I., Vanderlei Martins, J., Remer, L. A. and Afargan, H.: Smoke invigoration versus inhibition of clouds over the amazon, *Science*, 321(5891), 946–949, doi:10.1126/science.1159185, 2008.
- 20 Koren, I., Feingold, G. and Remer, L. A.: The invigoration of deep convective clouds over the Atlantic: Aerosol effect, meteorology or retrieval artifact?, *Atmos. Chem. Phys.*, 10(18), 8855–8872, doi:10.5194/acp-10-8855-2010, 2010.
- Koren, I., Dagan, G. and Altartatz, O.: From aerosol-limited to invigoration of warm convective clouds, *Science*, 344(6188), 1143–1146, doi:10.1126/science.1252595, 2014.
- Koren, I., Altartatz, O. and Dagan, G.: Aerosol effect on the mobility of cloud droplets, *Environ. Res. Lett.*, 10(10),
25 doi:10.1088/1748-9326/10/10/104011, 2015.
- Lau, K. M. and Kim, K. M.: Observational relationships between aerosol and Asian monsoon rainfall, and circulation, *Geophys. Res. Lett.*, 33(21), 1–5, doi:10.1029/2006GL027546, 2006.
- Lee, S. S., Donner, L. J., Phillips, V. T. J. and Ming, Y.: The dependence of aerosol effect on clouds and precipitation on cloud-system organization, shear and stability, *J. Geophys. Res. Atmos.*, 113(16), doi:10.1029/2007JD009224, 2008.
- 30 Li, G., Wang, Y. and Zhang, R.: Implementation of a two-moment bulk microphysics scheme to the WRF model to investigate aerosol-cloud interaction, *J. Geophys. Res. Atmos.*, 113(15), doi:10.1029/2007JD009361, 2008.
- Li, Z., Niu, F., Fan, J., Liu, Y., Rosenfeld, D. and Ding, Y.: Long-term impacts of aerosols on the vertical development of clouds and precipitation, *Nat. Geosci.*, 4(12), 888–894, doi:10.1038/ngeo1313, 2011.
- Li Z., W.K.-M. Lau, V. Ramanathan, G. Wu, Y. Ding, M.G. Manoj, J. Liu, Y. Qian, J. Li, T. Zhou, J. Fan, D. Rosenfeld, Y.

- Ming, Y., Wang, J., Huang, B., Wang, X., Xu, S.-S., Lee, M., Cribb, F., Zhang, X., Yang, Takemura, K., Wang, X., Xia, Y., Yin, H., Zhang, J., Guo, P.M., Zhai, N., Sugimoto, S., S. Babu, G.P., Brasseur: Aerosol and monsoon climate interactions over Asia, *Rev. Geophys.*, 54(4): 866–929, doi: 10.1002/2015RG000500, 2016.
- 5 Lin, J. C., Matsui, T., Pielke, S. A. and Kummerow, C.: Effects of biomass-burning-derived aerosols on precipitations and clouds in the Amazon Basin: A satellite-based empirical study, *J. Geophys. Res. Atmos.*, 111(19), doi:10.1029/2005JD006884, 2006.
- Lin, Y., Wang, Y., Pan, B., Hu, J., Liu, Y. and Zhang, R.: Distinct Impacts of Aerosols on an Evolving Continental Cloud Complex during the RACORO Field Campaign, *J. Atmos. Sci.*, doi:10.1175/JAS-D-15-0361.1, 2016.
- 10 Liu, H., Jacob, D. J., Bey, I. and Yantosca, R. M.: Constraints from 210 Pb and 7 Be on wet deposition and transport in a global three-dimensional chemical tracer model driven by assimilated meteorological fields, *J. Geophys. Res. Atmos.*, 106(D11), 12109–12128, doi:10.1029/2000JD900839, 2001.
- Liu, Z., Yim, S. H. L., Wang, C. and Lau, N. C.: The impact of the aerosol direct radiative forcing on deep convection and air quality in the Pearl River Delta Region, *Geophys. Res. Lett.*, doi:10.1029/2018GL077517, 2018.
- 15 Madronich, S.: Photodissociation in the atmosphere: 1. Actinic flux and the effects of ground reflections and clouds, *J. Geophys. Res.*, 92(D8), 9740, doi:10.1029/JD092iD08p09740, 1987.
- Morrison, H., Thompson, G. and Tatarskii, V.: Impact of cloud microphysics on the development of trailing stratiform precipitation in a simulated squall line: Comparison of one- and two-moment schemes, *Mon. Weather Rev.*, 137(3), 991–1007, doi:10.1175/2008MWR2556.1, 2009.
- Otte, T. L., Pouliot, G., Pleim, J. E., Young, J. O., Schere, K. L., Wong, D. C., Lee, P. C. S., Tsidulko, M., McQueen, J. T., 20 Davidson, P., Mathur, R., Chuang, H.-Y., DiMego, G. and Seaman, N. L.: Linking the eta model with the community multiscale air quality (CMAQ) modeling system to build a national air quality forecasting system, *Weather Forecast.*, 20(3), 367–384, doi:10.1175/WAF855.1, 2005.
- Qin, Y., Chen, Z., Shen, Y., Zhang, S. and Shi, R.: Evaluation of satellite rainfall estimates over the Chinese Mainland, *Remote Sens.*, 6(11), 11649–11672, doi:10.3390/rs61111649, 2014.
- 25 Rosenfeld, D.: Suppression of rain and snow by urban and industrial air pollution, *Science*, 287(5459), 1793–1796, doi:10.1126/science.287.5459.1793, 2000.
- Rosenfeld, D.: Aerosol-cloud interactions control of earth radiation and latent heat release budgets, *Space Sci. Rev.*, 125(1–4), 149–157, doi:10.1007/s11214-006-9053-6, 2006.
- Rosenfeld, D. and Woodley, W.: Deep convective clouds with sustained supercooled liquid water down to -37.5 degrees C, 30 *Nature*, 405(6785), 440–2, doi:10.1038/35013030, 2000.
- Rosenfeld, D., Kaufman, Y. J. and Koren, I.: Switching cloud cover and dynamical regimes from open to closed Benard cells in response to the suppression of precipitation by aerosols, *Atmos. Chem. Phys.*, 6(9), 2503–2511, doi:10.5194/acp-6-2503-2006, 2006.
- Rosenfeld, D., Lohmann, U., Raga, G. B., O’Dowd, C. D., Kulmala, M., Fuzzi, S., Reissell, A. and Andreae, M. O.: Flood or

- drought: How do aerosols affect precipitation?, *Science*, 321(5894), 1309–1313, doi:10.1126/science.1160606, 2008.
- Skamarock, W. C., Klemp, J. B., Dudhia, J., Gill, D. O., Barker, D. M., Duda, M. G., Huang, X.-Y., Wang, W. and Powers, J. G.: A description of the advanced research WRF version 3. [online] Available from: <https://pdfs.semanticscholar.org/ace5/4d4d1d6c9914997ad8f4e410044fdeb95b9d.pdf> (Accessed 15 May 2018), 2008.
- 5 Small, J. D., Chuang, P. Y., Feingold, G. and Jiang, H.: Can aerosol decrease cloud lifetime?, *Geophys. Res. Lett.*, 36(16), doi:10.1029/2009GL038888, 2009.
- Storer, R. L. and van den Heever, S. C.: Microphysical processes evident in aerosol forcing of tropical deep convective clouds, *J. Atmos. Sci.*, 70(2), 430–446, doi:10.1175/JAS-D-12-076.1, 2013.
- Tao, W. K., Li, X., Khain, A., Matsui, T., Lang, S. and Simpson, J.: Role of atmospheric aerosol concentration on deep
10 convective precipitation: Cloud-resolving model simulations, *J. Geophys. Res. Atmos.*, 112(24), doi:10.1029/2007JD008728, 2007.
- Tao, W. K., Chen, J. P., Li, Z., Wang, C. and Zhang, C.: Impact of aerosols on convective clouds and precipitation, *Rev. Geophys.*, 50(2), doi:10.1029/2011RG000369, 2012.
- Twomey, S.: The Influence of pollution on the shortwave albedo of clouds, *J. Atmos. Sci.*, 34(7), 1149–1152,
15 doi:10.1175/1520-0469(1977)034<1149:TIOPOT>2.0.CO;2, 1977.
- Wang, C.: A modeling study of the response of tropical deep convection to the increase of cloud condensation nuclei concentration: 1. Dynamics and microphysics, *J. Geophys. Res. Atmos.*, 110(21), 1–16, doi:10.1029/2004JD005720, 2005.
- Wang, Y., Wan, Q., Meng, W., Liao, F., Tan, H. and Zhang, R.: Long-term impacts of aerosols on precipitation and lightning over the Pearl River Delta megacity area in China, *Atmos. Chem. Phys.*, 11(23), 12421–12436, doi:10.5194/acp-11-12421-
20 2011, 2011.
- Wang, Y., Lee, K. H., Lin, Y., Levy, M. and Zhang, R.: Distinct effects of anthropogenic aerosols on tropical cyclones, *Nat. Clim. Chang.*, doi:10.1038/nclimate2144, 2014.
- Wang, Y., Ma, P. L., Jiang, J. H., Su, H. and Rasch, P. J.: Toward reconciling the influence of atmospheric aerosols and greenhouse gases on light precipitation changes in Eastern China, *J. Geophys. Res.*, doi:10.1002/2016JD024845, 2016.
- 25 Wang, Y., Vogel, J. M., Lin, Y., Pan, B., Hu, J., Liu, Y., Dong, X., Jiang, J. H., Yung, Y. L. and Zhang, R.: Aerosol microphysical and radiative effects on continental cloud ensembles, *Adv. Atmos. Sci.*, doi:10.1007/s00376-017-7091-5, 2018.
- Wiedinmyer, C., Akagi, S. K., Yokelson, R. J., Emmons, L. K., Al-Saadi, J. A., Orlando, J. J. and Soja, A. J.: The Fire INventory from NCAR (FINN) – a high resolution global model to estimate the emissions from open burning, *Geosci. Model Dev. Discuss.*, 3(4), 2439–2476, doi:10.5194/gmdd-3-2439-2010, 2010.
- 30 Wu, D., Tie, X., Li, C., Ying, Z., Lau, A. K. H., Huang, J., Deng, X. and Bi, X.: An extremely low visibility event over the Guangzhou region: A case study, *Atmos. Environ.*, 39(35), 6568–6577, doi:10.1016/j.atmosenv.2005.07.061, 2005.
- Xie, P., Joyce, R., Wu, S., Yoo, S.-H., Yarosh, Y., Sun, F. and Lin, R.: Reprocessed, bias-corrected CMORPH global high-resolution precipitation estimates from 1998, *J. Hydrometeorol.*, 18(6), 1617–1641, doi:10.1175/JHM-D-16-0168.1, 2017.

- Yang, Q., Gustafson, W. I., Fast, J. D., Wang, H., Easter, R. C., Morrison, H., Lee, Y. N., Chapman, E. G., Spak, S. N. and Mena-Carrasco, M. A.: Assessing regional scale predictions of aerosols, marine stratocumulus, and their interactions during VOCALS-REx using WRF-Chem, *Atmos. Chem. Phys.*, 11(23), 11951–11975, doi:10.5194/acp-11-11951-2011, 2011.
- Zaveri, R. A. and Peters, L. K.: A new lumped structure photochemical mechanism for large-scale applications, *J. Geophys. Res. Atmos.*, 104(D23), 30387–30415, doi:10.1029/1999JD900876, 1999.
- Zaveri, R. A., Easter, R. C., Fast, J. D. and Peters, L. K.: Model for simulating aerosol interactions and chemistry (MOSAIC), *J. Geophys. Res. Atmos.*, 113(13), doi:10.1029/2007JD008782, 2008.
- Zhang, Y. L., and F. Cao: Fine particulate matter (PM_{2.5}) in China at a city level. *Sci. Rep.*, 5, 14884, <https://doi.org/10.1038/srep14884>, 2015.
- 10 Zhao, C., Wang, Y., Choi, Y. and Zeng, T.: Summertime impact of convective transport and lightning NO_x production over North America: Modeling dependence on meteorological simulations, *Atmos. Chem. Phys.*, 9(13), 4315–4327, doi:10.5194/acp-9-4315-2009, 2009.
- Zhao, C., Liu, X., Leung, L. R., Johnson, B., Mcfarlane, S. A., Jr, W. I. G., Fast, J. D. and Easter, R.: The spatial distribution of mineral dust and its shortwave radiative forcing over North Africa: modeling sensitivities to dust emissions and aerosol size treatments, *Atmos. Chem. Phys.*, 10, 8821–8838, doi:10.5194/acp-10-8821-2010, 2010.
- 15 Zhao, C., Liu, X., Leung, L. R. and Hagos, S.: and Physics Radiative impact of mineral dust on monsoon precipitation variability over West Africa, (2007), 1879–1893, doi:10.5194/acp-11-1879-2011, 2011.
- Zhao, C., Leung, L. R., Easter, R., Hand, J. and Avise, J.: Characterization of speciated aerosol direct radiative forcing over California, *J. Geophys. Res. Atmos.*, 118(3), 2372–2388, doi:10.1029/2012JD018364, 2013a.
- 20 Zhao, C., Chen, S., Leung, L. R., Qian, Y., Kok, J. F., Zaveri, R. A. and Huang, J.: Uncertainty in modeling dust mass balance and radiative forcing from size parameterization, *Atmos. Chem. Phys.*, 13(21), 10733–10753, doi:10.5194/acp-13-10733-2013, 2013b.
- Zhao, C., Hu, Z., Qian, Y., Ruby Leung, L., Huang, J., Huang, M., Jin, J., Flanner, M. G., Zhang, R., Wang, H., Yan, H., Lu, Z. and Streets, D. G.: Simulating black carbon and dust and their radiative forcing in seasonal snow: A case study over
- 25 North China with field campaign measurements, *Atmos. Chem. Phys.*, 14(20), 11475–11491, doi:10.5194/acp-14-11475-2014, 2014.
- Zhao, C., Huang, M., Fast, J. D., Berg, L. K., Qian, Y., Guenther, A., Gu, D., Shrivastava, M., Liu, Y., Walters, S., Pfister, G., Jin, J., Shilling, J. E. and Warneke, C.: Sensitivity of biogenic volatile organic compounds to land surface parameterizations and vegetation distributions in California, *Geosci. Model Dev.*, 9(5), 1959–1976, doi:10.5194/gmd-9-1959-2016, 2016.
- 30 Zhao, C., Lin, Y., Wu, F., Wang, Y., Li, Z., Rosenfeld, D. and Wang, Y.: Enlarging Rainfall Area of Tropical Cyclones by Atmospheric Aerosols, *Geophys. Res. Lett.*, doi:10.1029/2018GL079427, 2018.
- Zhong, S., Qian, Y., Zhao, C., Leung, R. and Yang, X. Q.: A case study of urbanization impact on summer precipitation in the greater Beijing metropolitan area: Urban heat island versus aerosol effects, *J. Geophys. Res.*, 120(20), 10,903-10,914, doi:10.1002/2015JD023753, 2015.

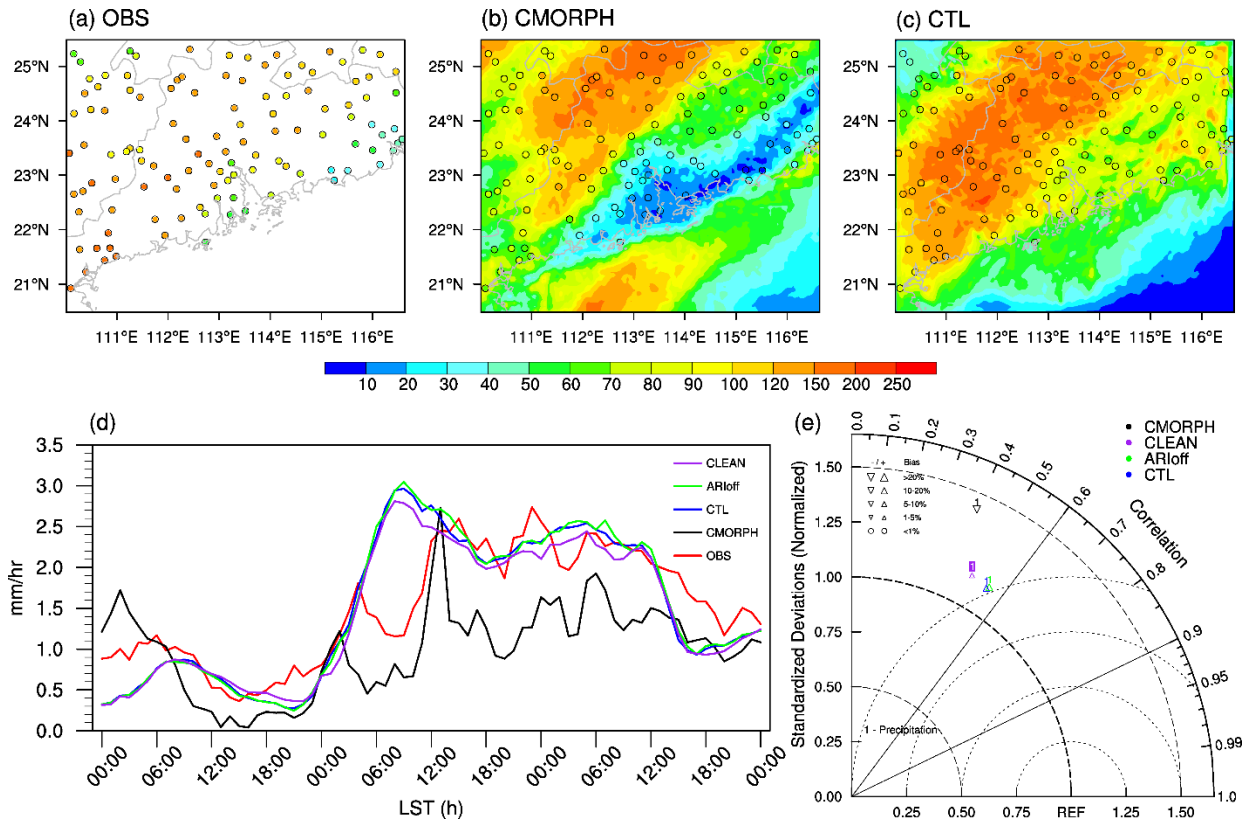
Zhong, S., Qian, Y., Zhao, C., Leung, R., Wang, H., Yang, B., Fan, J., Yan, H., Yang, X. Q. and Liu, D.: Urbanization-induced urban heat island and aerosol effects on climate extremes in the Yangtze River Delta region of China, *Atmos. Chem. Phys.*, 17(8), 5439–5457, doi:10.5194/acp-17-5439-2017, 2017.



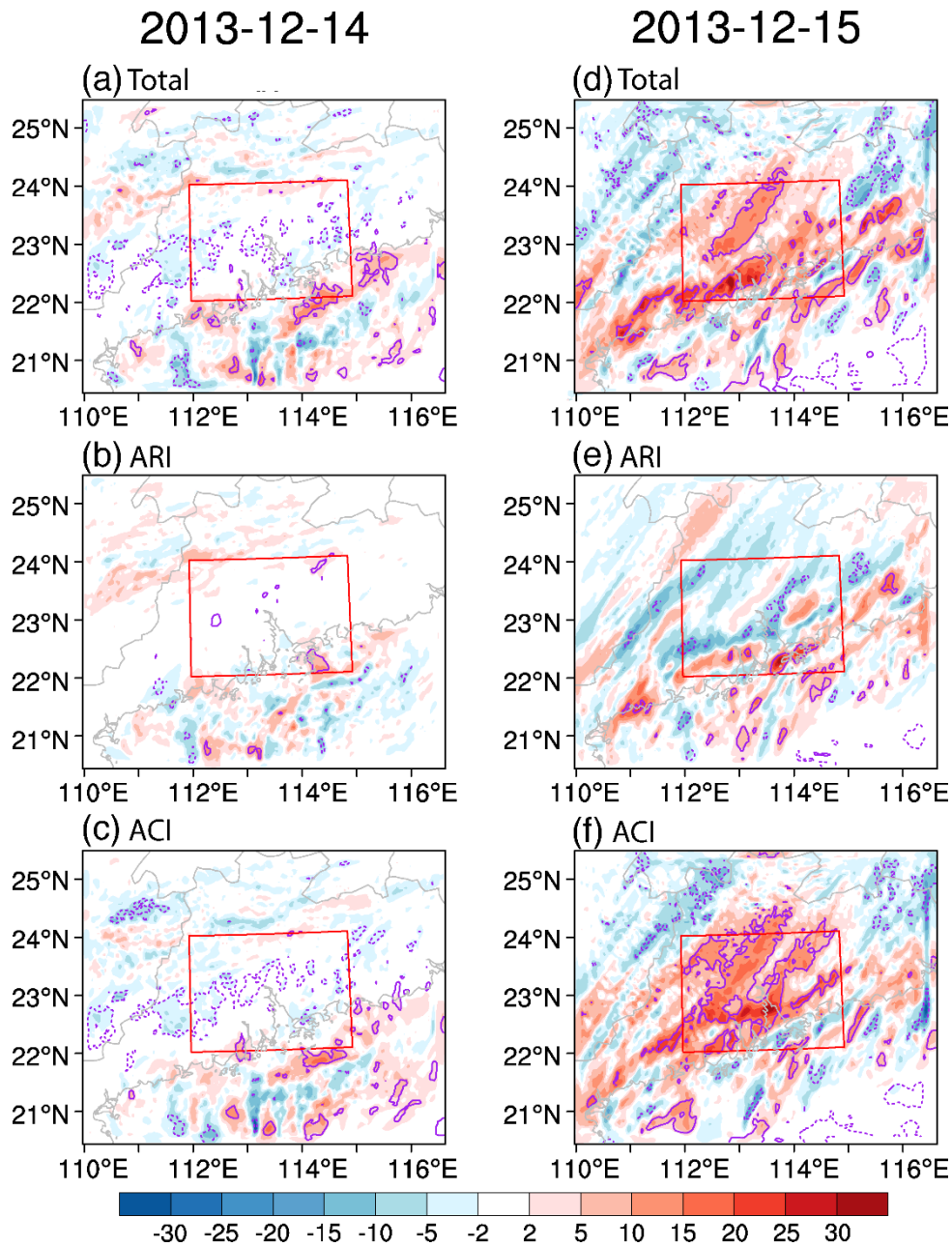
5

Figure 1. (a) Terra satellite true-color image of east China on December 13, 2013 (UTC), provided by NASA's Worldview (source: <https://worldview.earthdata.nasa.gov/>). Red circles denote city locations, blue fonts denote cities, and orange fonts in bold italic denote provinces. (b) Spatial distribution of 3-day averaged column-integrated PM_{2.5} concentrations (shading; unit: $\mu\text{g m}^{-2}$) and 925-hPa wind (vector; unit: m s^{-1}) during December 14–16, 2013, in control run. The red box denotes the analysis region. (c) Hourly-averaged PM_{2.5} (unit: $\mu\text{g m}^{-3}$) concentration on December 13, 2013, observed in Guangdong province. Colored circles denote in situ station locations, and black star denotes Guangzhou.

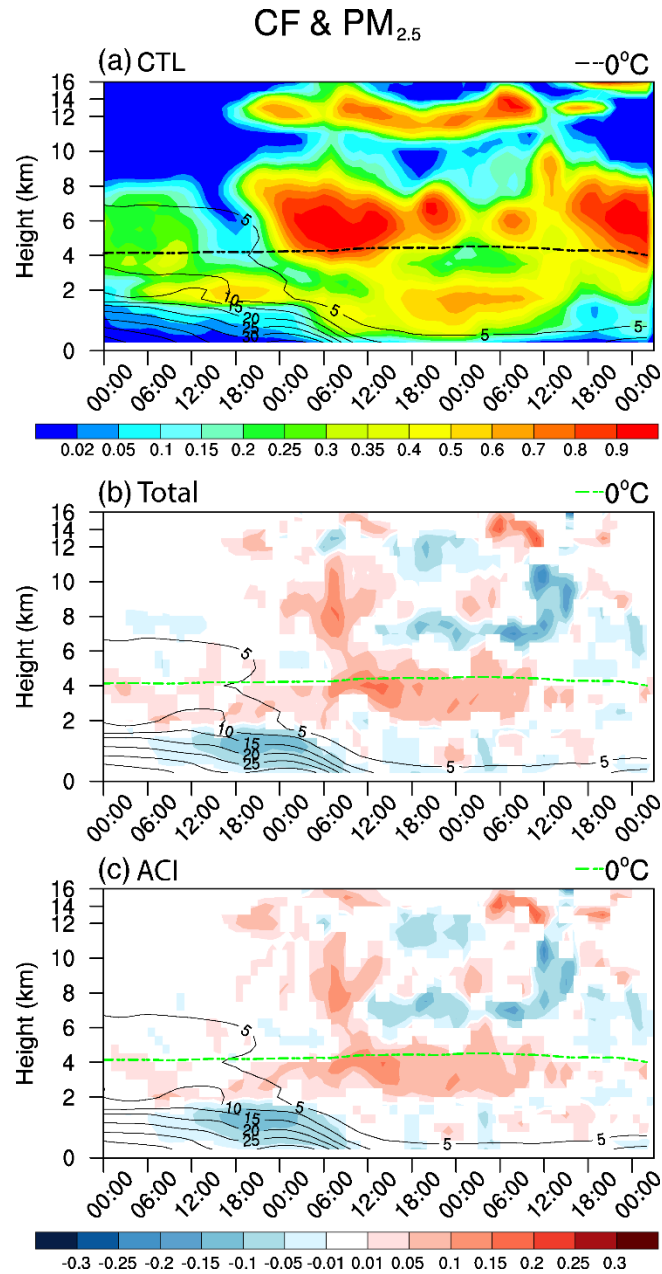
10



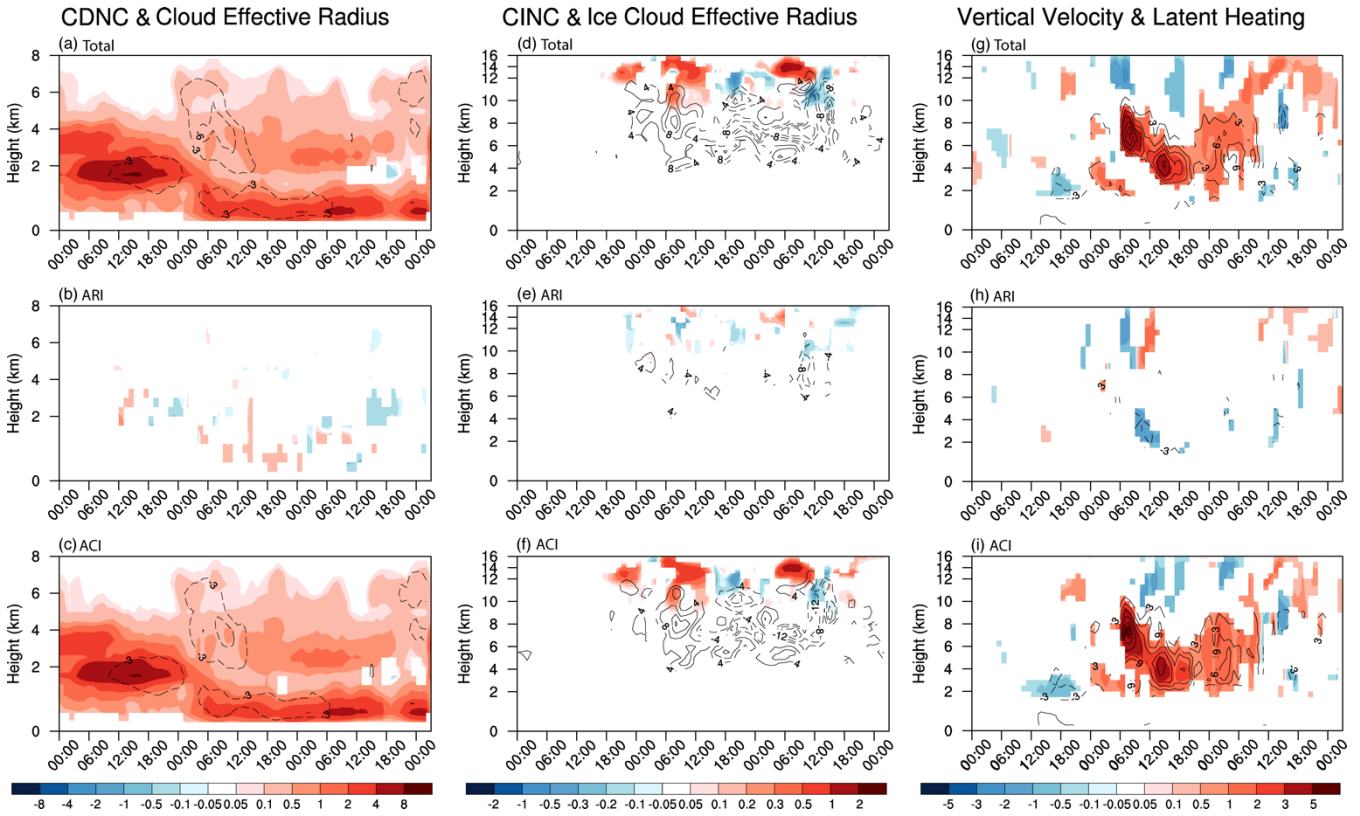
5 **Figure 2.** Spatial distribution of accumulated precipitation (unit: mm) from 00Z on December 14, 2013, to 00Z on December 17, 2013 (local standard time [LST]) from (a) station observations (OBS), (b) CMORPH satellite, (c) control simulation (CTL). Circles denote locations of in situ observations. (d) Time series of station average of rain rate (unit: mm h⁻¹) over the entire domain 2 for OBS (red), CMORPH (black), and CTL (blue). (e) Taylor diagrams for 3-day accumulated precipitation in CTL (blue) and CMORPH (black) compared with OBS. Triangles and circles at top-left corner in (e) denote bias. Sizes of triangles indicate magnitude of bias. Inverted (upright) triangles represent a negative (positive) bias.



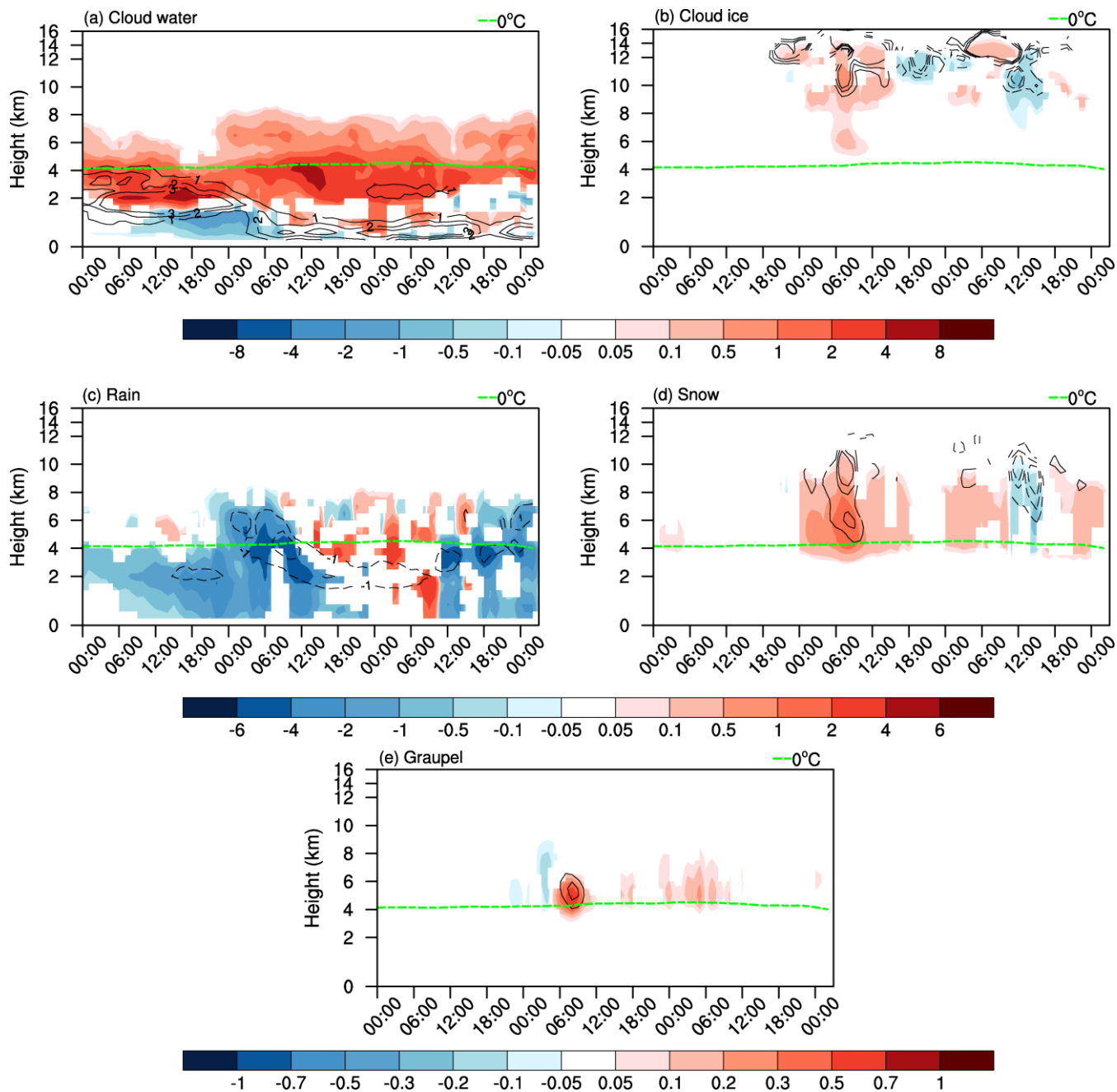
5 **Figure 3.** Differences in precipitation (unit: mm) (a) between CTL and CLEAN (i.e., CTL minus CLEAN), (b) CTL and ARloff (i.e., CTL minus ARloff), and (c) ARloff and CLEAN (i.e., ARloff minus CLEAN; third row) on December 14. (c–f) Same as (a–c) but for December 15. Solid (dashed) purple contour lines indicate positive (negative) differences at the 90% significance level according to two-tailed Student’s *t* test. Red boxes (22°–24° N, 112°–115° E) denote the analysis region. ARloff run refers to simulation with aerosol-radiation interactions off.



5 **Figure 4.** (a) Time-height cross section of cloud fraction (CF; shading; unit: unitless) and PM_{2.5} concentrations (contour; unit: $\mu\text{g m}^{-3}$) averaged over the red box shown in Figure 3 in CTL run. Differences in the time-height cross section of CF (shading; unit: unitless) and PM_{2.5} concentration (contour; unit: $\mu\text{g m}^{-3}$) averaged over the red box shown in Figure 3 between (b) CTL and CLEAN (i.e., CTL minus CLEAN) and (c) ARIoff and CLEAN (i.e., ARIoff minus CLEAN). In (b) and (c), only CF and PM_{2.5} concentrations anomalies that exceed the 90% significance level are depicted with shading and contour, respectively. Dashed lines denote 0°C isotherm calculated as the averaged zero-layer height over the red box in Figure 3.



5 **Figure 5.** Differences with time (abscissa; from 00Z on December 14 to 02Z on December 17) and height (ordinate) in (a) cloud droplet number concentration (CDNC, shading; unit: 10^7 kg^{-1}) and cloud effective radius (contour; unit: μm), (d) cloud ice number concentration (CINC, shading; unit: 10^5 kg^{-1}) and ice cloud effective radius (contour; unit: μm), and (g) vertical velocity (shading; unit: cm s^{-1}) and latent heating (contour; unit: K d^{-1}) averaged over the red box shown in Figure 3 between CTL and CLEAN (i.e., CTL minus CLEAN; first row). (b, e, h) Same as (a, d, g) but for differences between CTL and ARIoff (i.e., CTL minus ARIoff; second row). (c, f, i) Same as (a, d, g) but for differences between ARIoff and CLEAN (i.e., ARIoff minus CLEAN; third row). Only anomalies that exceed the 90% significance level are depicted with shading or contour. Zero-value contour lines are omitted, and negative values are dashed.



5 **Figure 6.** Differences with time (abscissa) and height (ordinate) in (a) cloud water (shading; unit: $10^{-5} \text{ kg kg}^{-1}$) and CDNC (contour; unit: 10^7 kg^{-1}), (b) cloud ice (shading; unit: $10^{-5} \text{ kg kg}^{-1}$) and CINC (contour; unit: 10^4 kg^{-1}), (c) rain (shading; unit: $10^{-5} \text{ kg kg}^{-1}$) and rain number concentration (contour; unit: 10^5 kg^{-1}), (d) snow (shading; unit: $10^{-4} \text{ kg kg}^{-1}$) and snow number concentrations (contour; unit: 10^3 kg^{-1}), and (e) graupel (shading; unit: $10^{-4} \text{ kg kg}^{-1}$) and graupel number concentration (contour; unit: 10^3 kg^{-1}) between CTL and CLEAN (i.e. CTL minus CLEAN) averaged over the red box. Only anomalies that exceed 90% significance level are depicted with shading and contour.

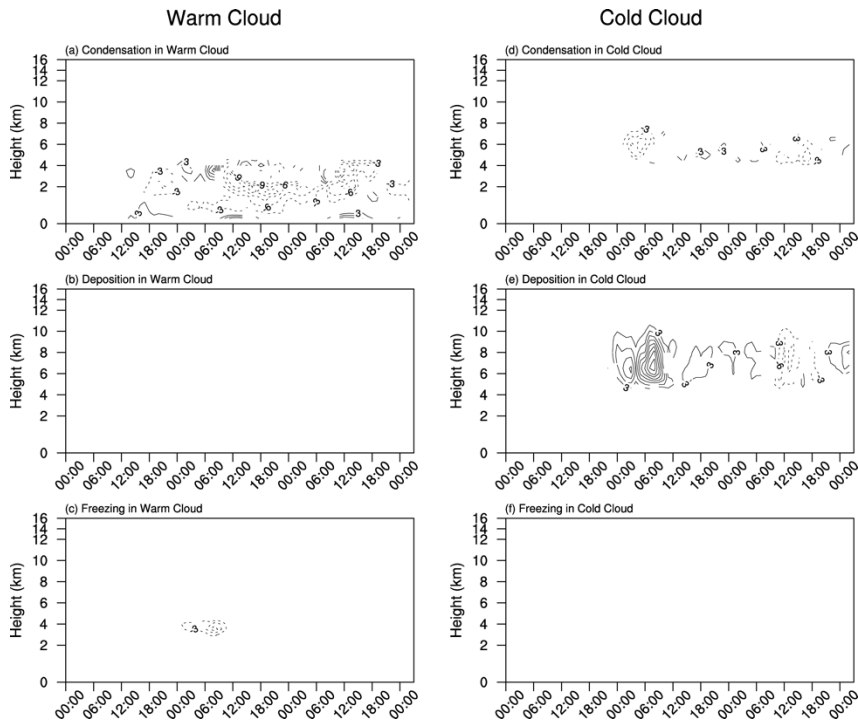


Figure 7. Differences with time (abscissa) and height (ordinate) in latent heat release (unit: K d^{-1}) from (a) condensation, (b) deposition, and (c) freezing processes between CTL and CLEAN (i.e. CTL minus CLEAN) averaged over the red box for the warm cloud. (d–f) Same as (a–c) but from cold cloud. Only anomalies that exceed 90% significance level are depicted with and contour. Zero-value contour lines are omitted, and negative values are dashed. The contour interval is 3 K d^{-1} . Note the blank represent the values are within 3 K d^{-1} .

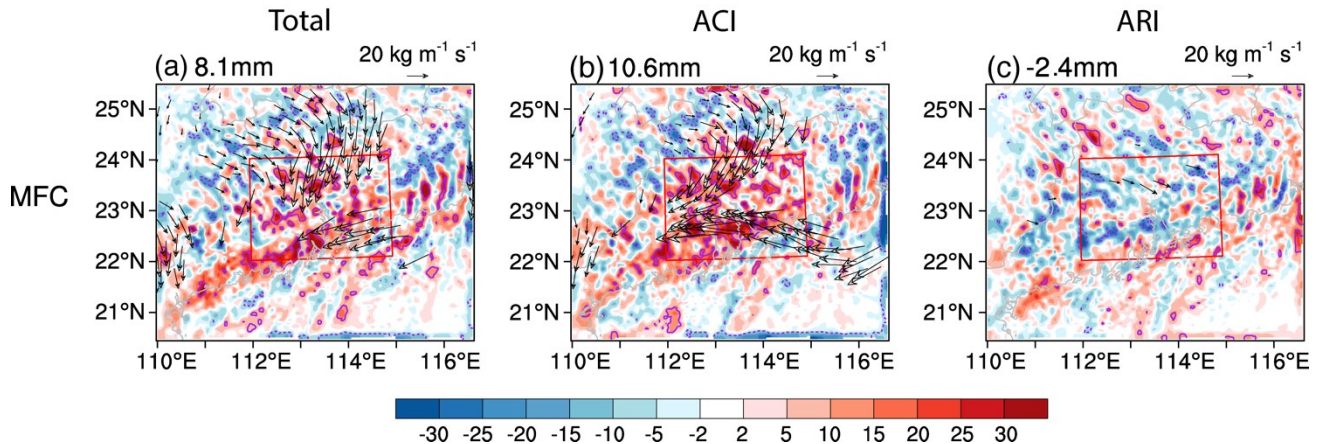
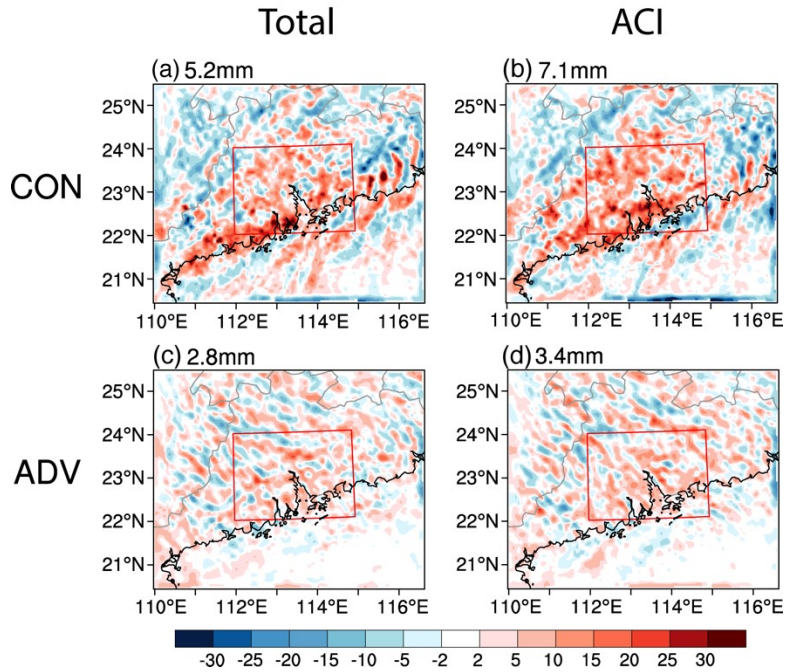


Figure 8. Differences in column-integrated flux convergence (MFC; shading; unit: mm) and moisture flux (vector; unit: $\text{kg m}^{-1} \text{ s}^{-1}$) between (a) CTL and CLEAN (i.e., CTL minus CLEAN), (b) ARIOff and CLEAN (i.e., ARIOff minus CLEAN), and (c) CTL and ARIOff (i.e. CTL minus ARIOff) on December 15. Solid (dashed) purple contour lines indicate positive (negative) differences (shading) at the 90% significance level according to two-tailed Student's t test. Only moisture flux anomalies that exceed the 90%

significance level are depicted with black vectors. Numbers at top-left corner of each panel represent values averaged over red boxes. Red boxes (22° – 24° N, 112° – 115° E) denote the analysis region.



5 **Figure 9.** Differences in column-integrated moisture convergence (CON; unit: mm) between (a) CTL and CLEAN (i.e. CTL minus CLEAN) and (b) ARloff and CLEAN (i.e., ARloff minus CLEAN) on December 15. (c, d) Same as (a, b) but for column-integrated advection of water vapor (ADV; unit: mm). The numbers at the top-left corner of each panel represent the values averaged over the red boxes. The red boxes denote the analysis region.

CF & PM_{2.5}

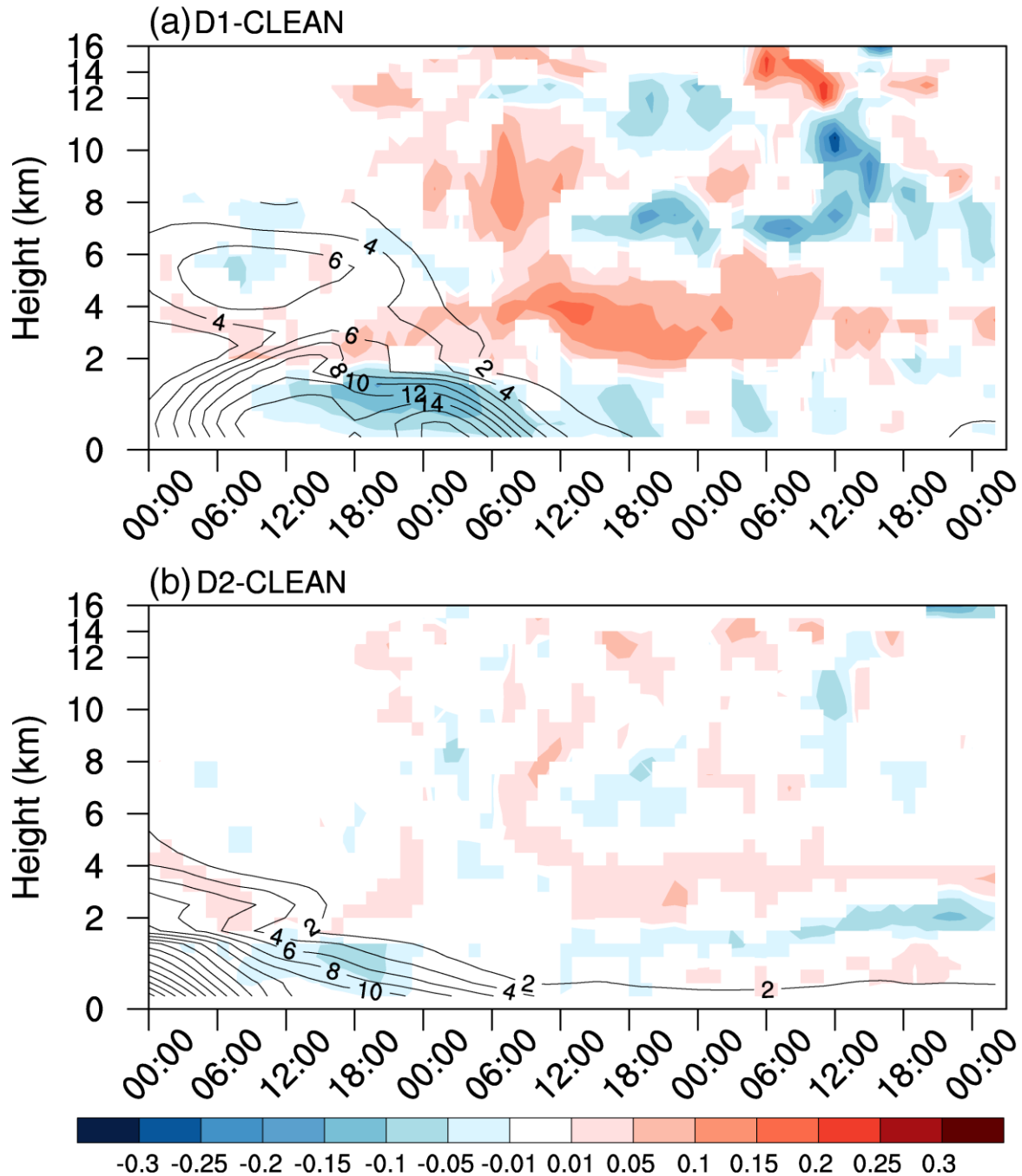
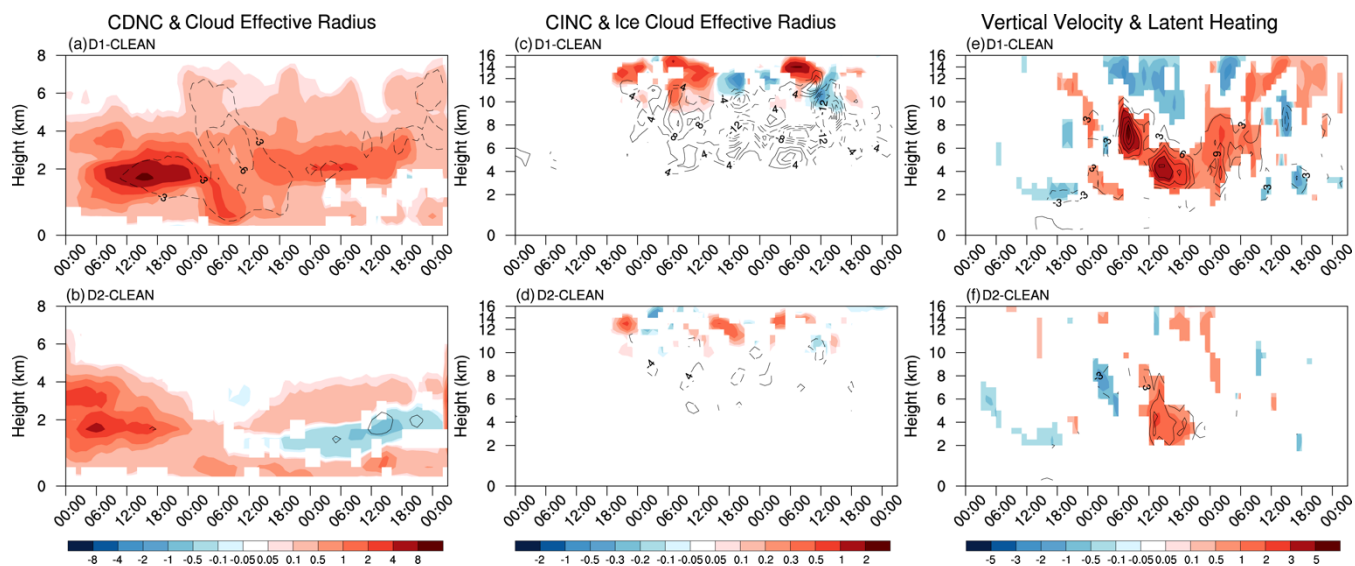
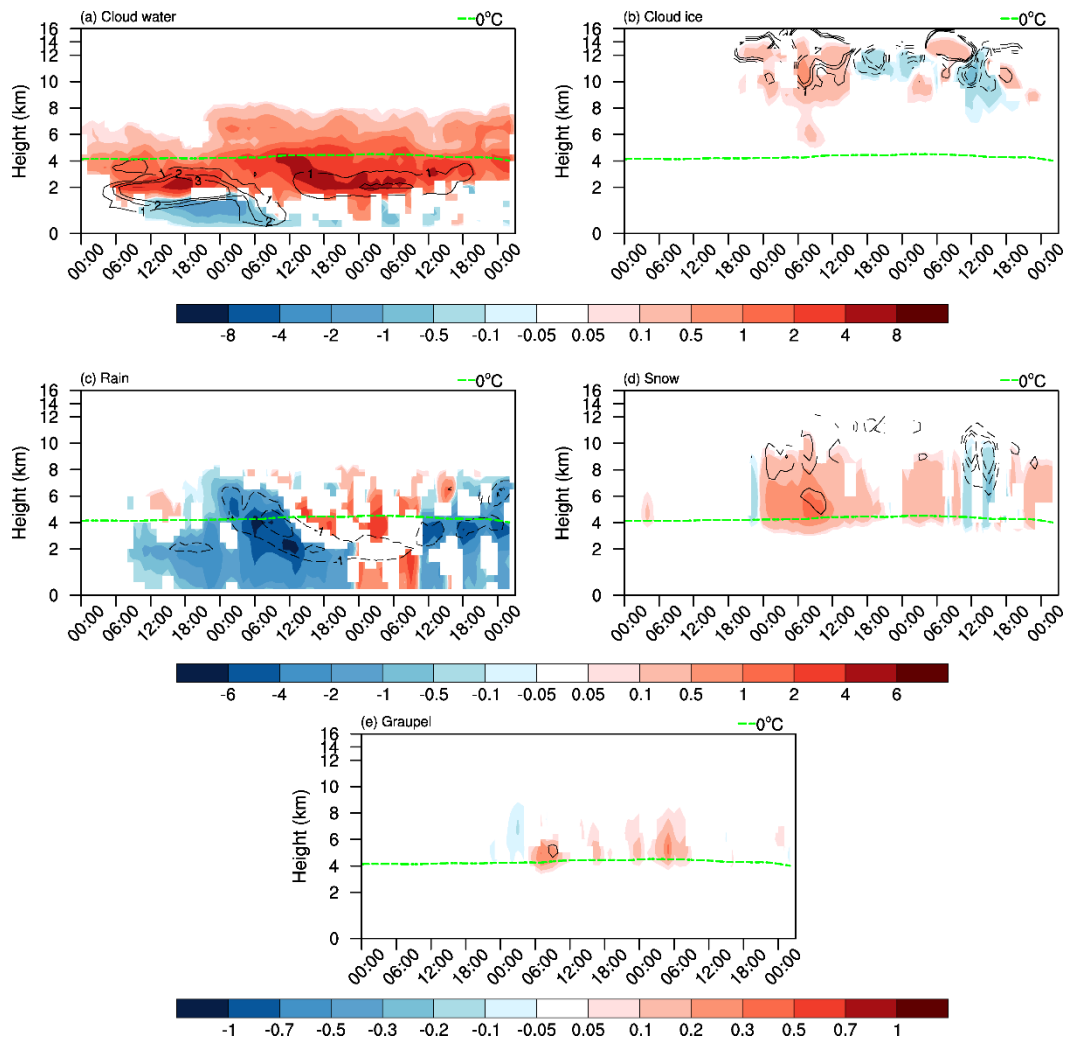


Figure 10. Differences in time-height cross section of CF (shading; unit: unitless) and PM_{2.5} concentration (contour; unit: $\mu\text{g m}^{-3}$) averaged over the red box shown in Figure 3 between (a) D1 and CLEAN (i.e., D1 minus CLEAN) and (b) D2 and CLEAN (i.e., D2 minus CLEAN). Only CF and PM_{2.5} concentrations anomalies that exceed the 90% significance level are depicted with shading and contour, respectively.

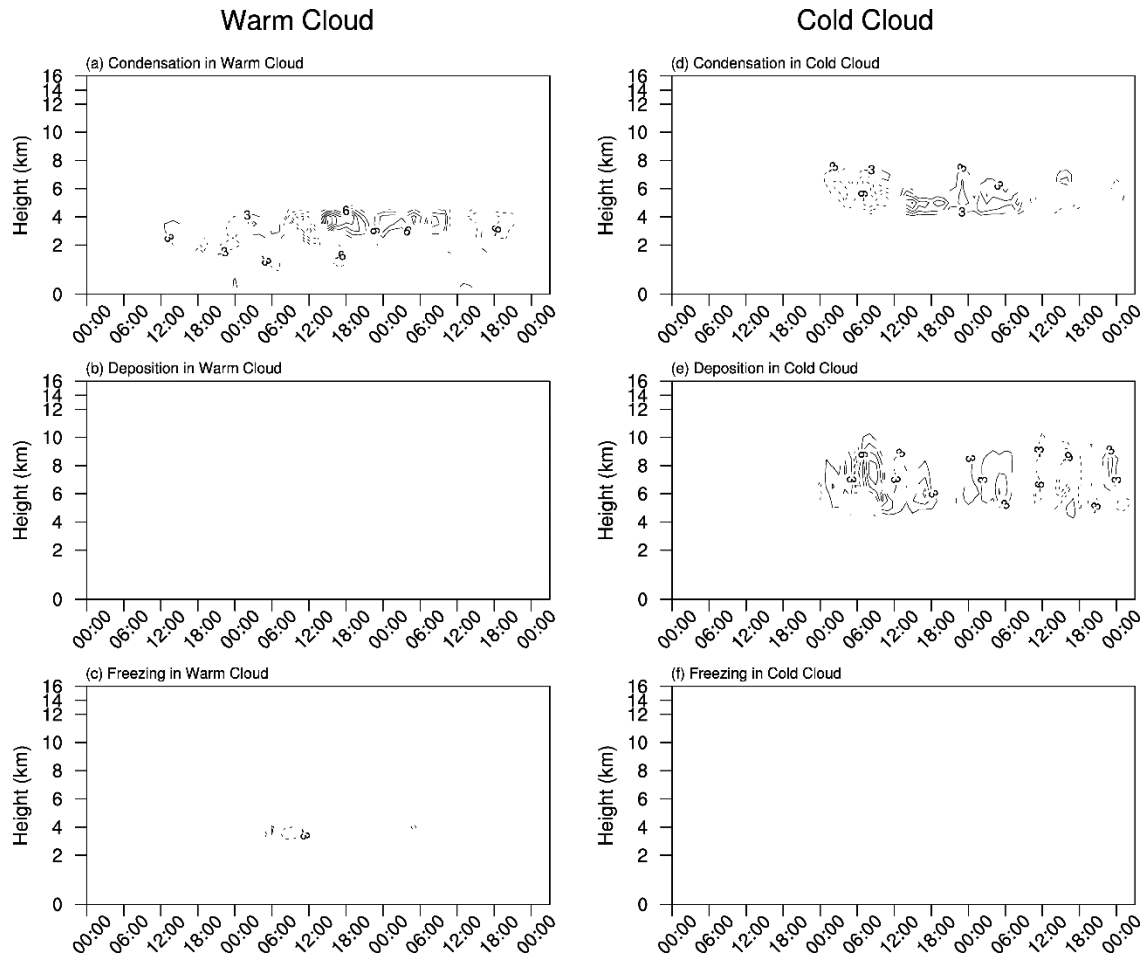
5



5 **Figure 11.** Differences with time (abscissa; from 00Z on December 14 to 02Z on December 17) and height (ordinate) in (a) CDNC (shading; unit: 10^7 kg^{-1}) and cloud effective radius (contour; unit: μm), (c) CINC (shading; unit: 10^5 kg^{-1}) and ice cloud effective radius (contour; unit: μm), and (e) vertical velocity (shading; unit: cm s^{-1}) and latent heating (contour; unit: K d^{-1}) averaged over the red box shown in Figure 3 between D1 and CLEAN (i.e., D1 minus CLEAN; first row). (b, d, f) same as (a, c, e) but for differences between D2 and CLEAN (i.e., D2 minus CLEAN; second row). Only anomalies that exceed the 90% significance level are depicted with shading or contour. Zero-value contour lines are omitted, and negative values are dashed.



5 **Figure 12.** Differences with time (abscissa) and height (ordinate) in (a) cloud water (shading; unit: $10^{-5} \text{ kg kg}^{-1}$) and CDNC (contour; unit: 10^7 kg^{-1}), (b) cloud ice (shading; unit: $10^{-5} \text{ kg kg}^{-1}$) and CINC (contour; unit: 10^4 kg^{-1}), (c) rain (shading; unit: $10^{-5} \text{ kg kg}^{-1}$) and rain number concentration (contour; unit: 10^5 kg^{-1}), (d) snow (shading; unit: $10^{-4} \text{ kg kg}^{-1}$) and snow number concentrations (contour; unit: 10^3 kg^{-1}), and (e) graupel (shading; unit: $10^{-4} \text{ kg kg}^{-1}$) and graupel number concentration (contour; unit: 10^3 kg^{-1}) between D1 and CLEAN (i.e. D1 minus CLEAN) averaged over the red box. Only anomalies that exceed 90% significance level are depicted with shading and contour.



5 **Figure 13.** Differences with time (abscissa) and height (ordinate) in (a) cloud water (shading; unit: $10^{-5} \text{ kg kg}^{-1}$) and CDNC (contour; unit: 10^7 kg^{-1}), (b) cloud ice (shading; unit: $10^{-5} \text{ kg kg}^{-1}$) and CINC (contour; unit: 10^4 kg^{-1}), (c) rain (shading; unit: $10^{-5} \text{ kg kg}^{-1}$) and rain number concentration (contour; unit: 10^5 kg^{-1}), (d) snow (shading; unit: $10^{-4} \text{ kg kg}^{-1}$) and snow number concentrations (contour; unit: 10^3 kg^{-1}), and (e) graupel (shading; unit: $10^{-4} \text{ kg kg}^{-1}$) and graupel number concentration (contour; unit: 10^3 kg^{-1}) between D1 and CLEAN (i.e. D1 minus CLEAN) averaged over the red box. Only anomalies that exceed 90% significance level are depicted with shading and contour.

2013-12-14

2013-12-15

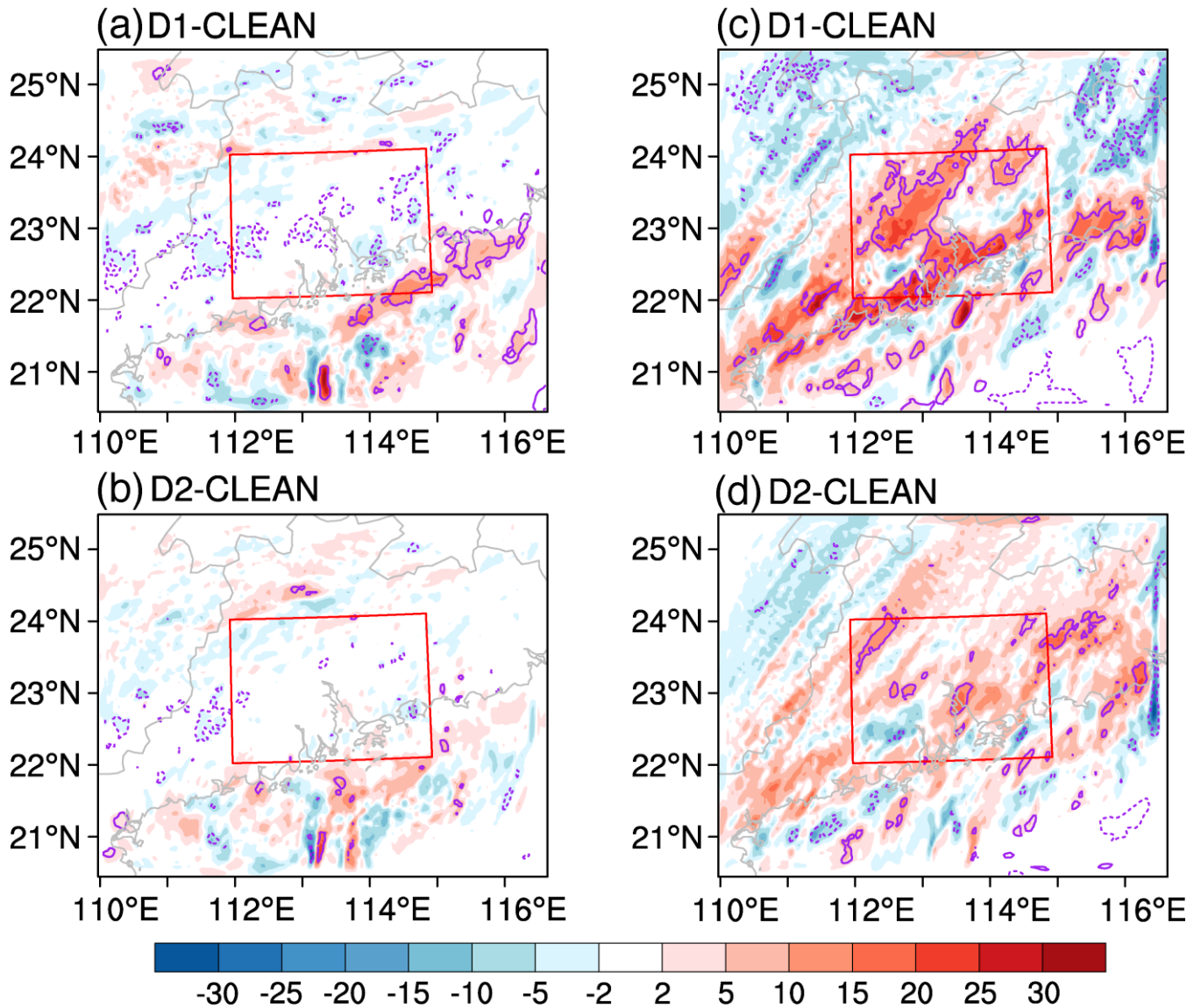


Figure 14. Differences in precipitation (unit: mm) between (a) D1 and CLEAN (i.e., D1 minus CLEAN) and (b) D2 and CLEAN (i.e., D2 minus CLEAN) on December 14. (c, d) Same as (a, b) but for December 15 (right column). Solid (dashed) purple contour lines indicate positive (negative) differences at the 90% significance according to two-tailed Student's t test. Red boxes (22°–24° N, 112°–115° E) denote the analysis region.

5

CF & PM_{2.5}

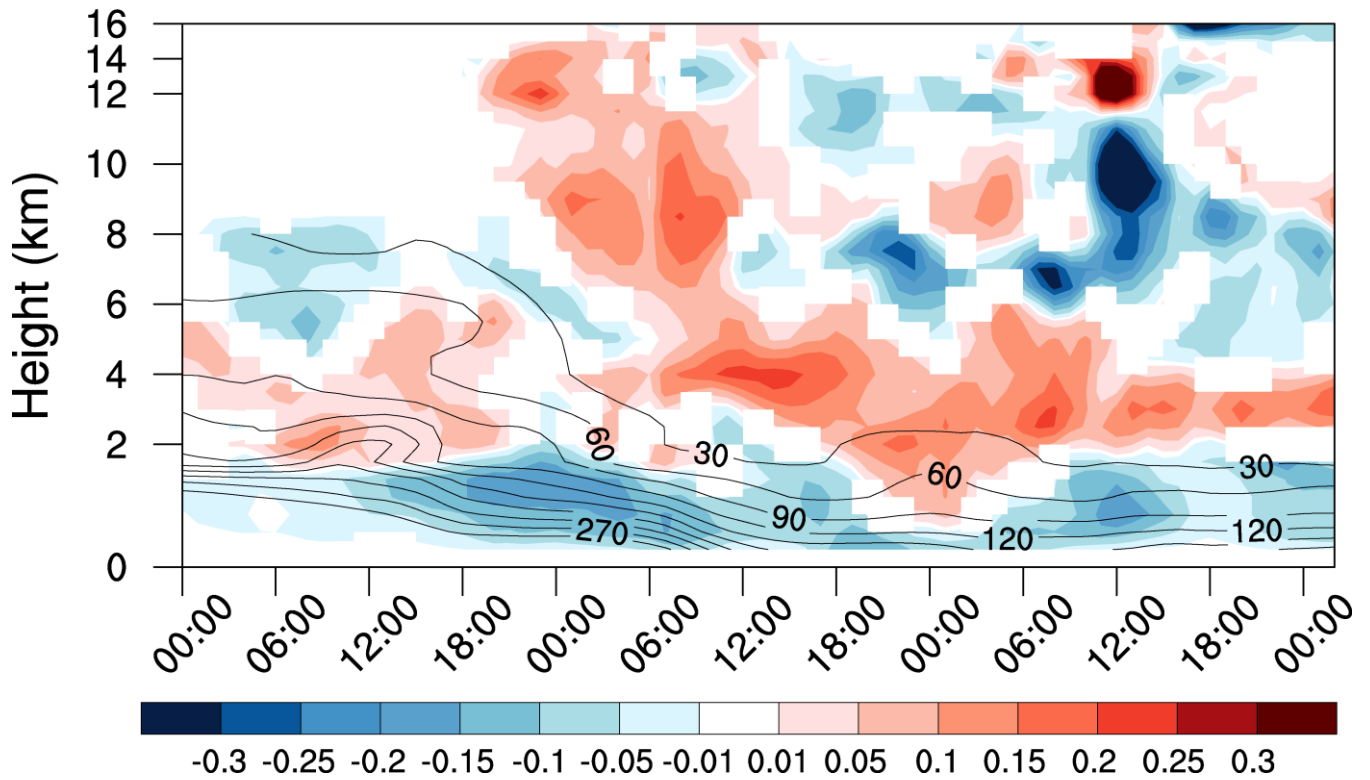
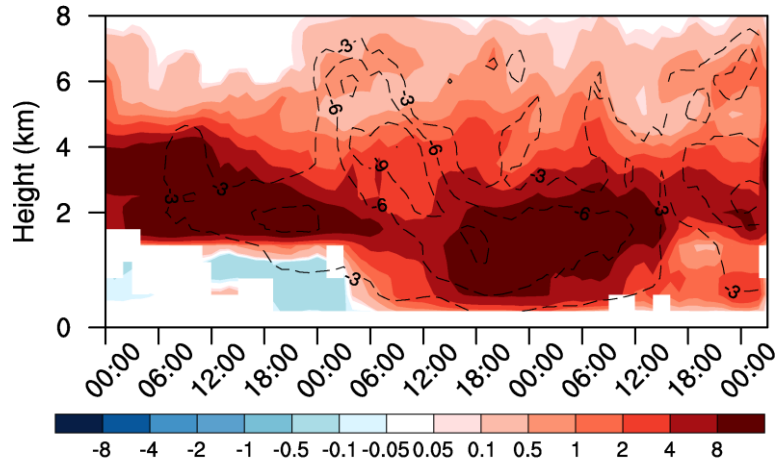
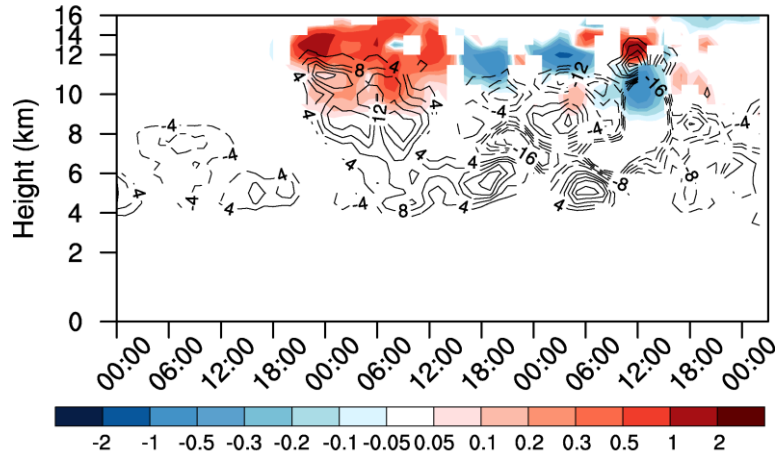


Figure 15. Differences in the time-height cross section of cloud factor CF (shading; unit: unitless) and PM_{2.5} concentrations (contour; unit: $\mu\text{g m}^{-3}$) averaged over the red box shown in Figure 3 between 10 \times and CLEAN (i.e., 10 \times minus CLEAN). Only CF and PM_{2.5} concentrations anomalies that exceed the 90% significance level are depicted with shading and contour, respectively.

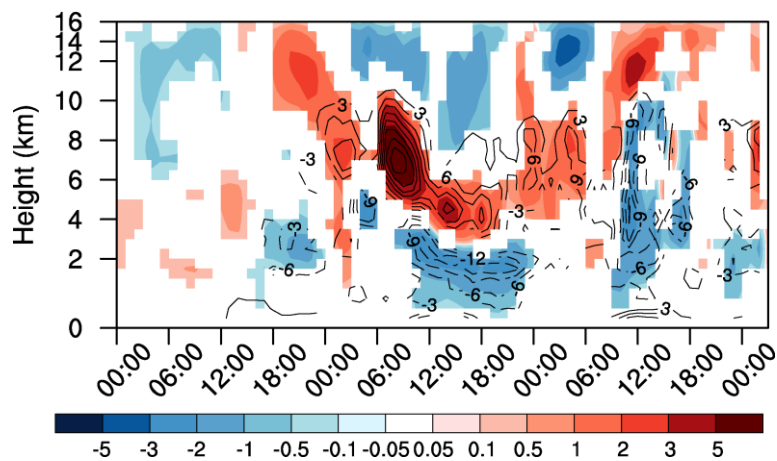
(a) CDNC & Cloud Effective Radius



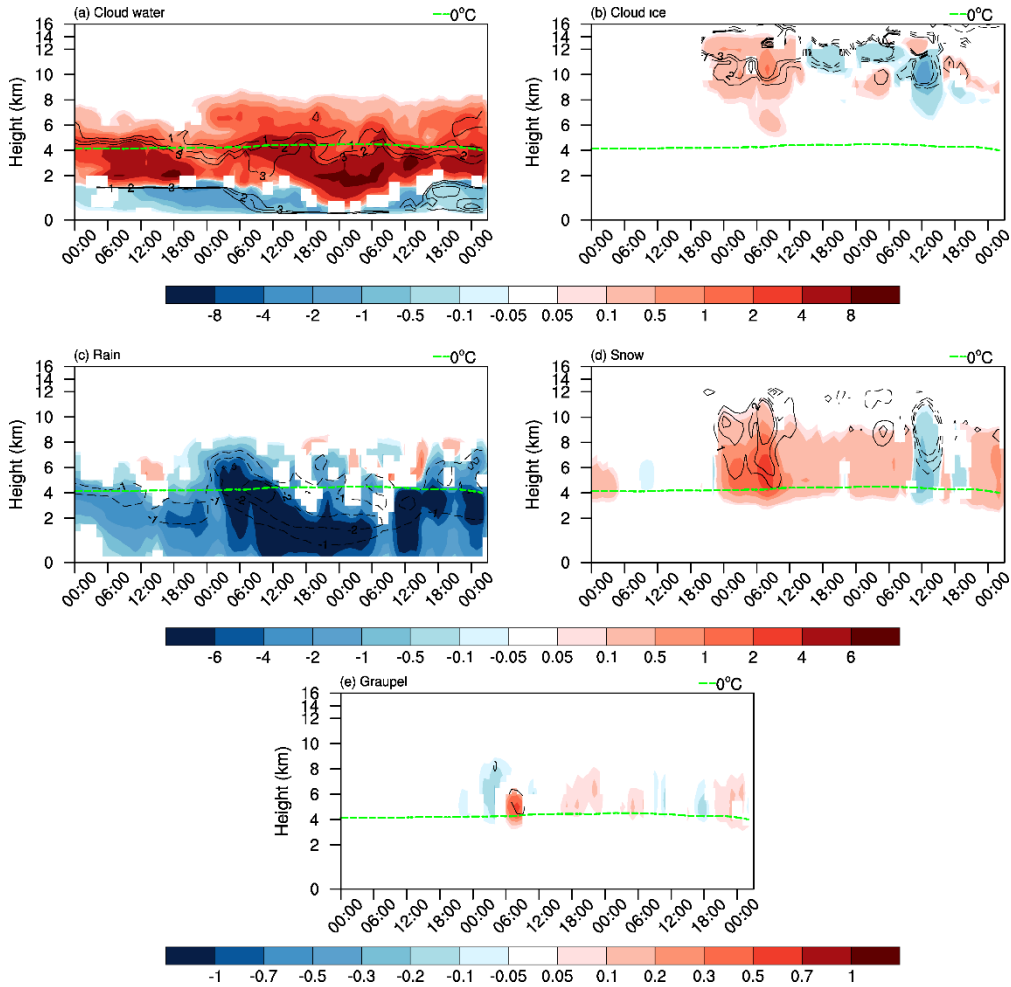
(b) CINC & Ice Cloud Effective Radius



(c) Vertical Velocity & Latent Heating



5 Figure 16. Differences with time (abscissa; from 00Z on December 14 to 02Z on December 17) and height (ordinate) in (a) CDNC (shading; unit: 10^7 kg^{-1}) and cloud effective radius (unit: μm), (b) CINC (shading; unit: 10^5 kg^{-1}) and ice cloud effective radius (contour; unit: μm), and (c) vertical velocity (shading; unit: cm s^{-1}) and latent heating (contour; unit: K d^{-1}) averaged over the red box shown in Figure 3 between $10\times$ and CLEAN (i.e., $10\times$ minus CLEAN). Only anomalies that exceed the 90% significance level are depicted with shading or contour. Zero-value contour lines are omitted, and negative values are dashed.



10 Figure 17. Differences with time (abscissa) and height (ordinate) in (a) cloud water (shading; unit: $10^{-5} \text{ kg kg}^{-1}$) and CDNC (contour; unit: 10^7 kg^{-1}), (b) cloud ice (shading; unit: $10^{-5} \text{ kg kg}^{-1}$) and CINC (contour; unit: 10^4 kg^{-1}), (c) rain (shading; unit: $10^{-5} \text{ kg kg}^{-1}$) and rain number concentration (contour; unit: 10^5 kg^{-1}), (d) snow (shading; unit: $10^{-4} \text{ kg kg}^{-1}$) and snow number concentrations (contour; unit: 10^3 kg^{-1}), and (e) graupel (shading; unit: $10^{-4} \text{ kg kg}^{-1}$) and graupel number concentration (contour; unit: 10^3 kg^{-1}) between $10\times$ and CLEAN (i.e. $10\times$ minus CLEAN) averaged over the red box. Only anomalies that exceed 90% significance level are depicted with shading and contour.

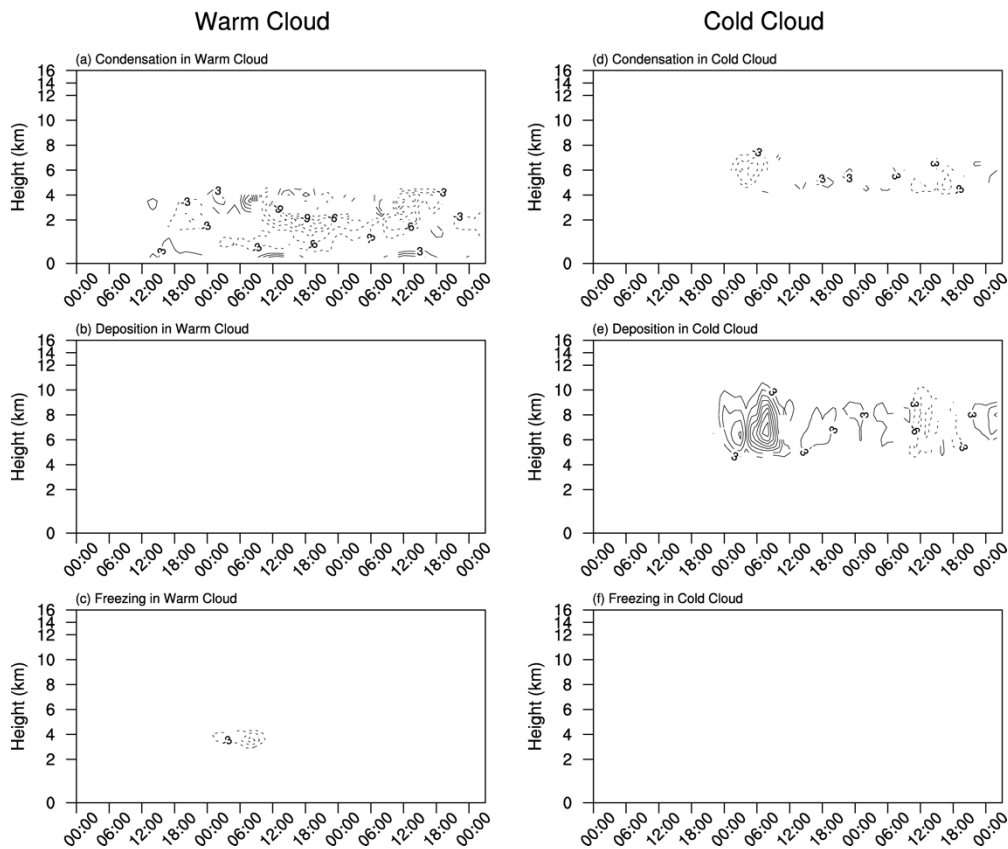


Figure 18. Differences with time (abscissa) and height (ordinate) in latent heat release (unit: K d^{-1}) from (a) condensation, (b) deposition, and (c) freezing processes between $10\times$ and CLEAN (i.e. $10\times$ minus CLEAN) averaged over the red box for the warm cloud. (d–f) Same as (a–c) but from cold cloud. Only anomalies that exceed 90% significance level are depicted with and contour. Zero-value contour lines are omitted, and negative values are dashed. The contour interval is 3 K d^{-1} . Note the blank represent the values are within 3 K d^{-1} .

Precipitation

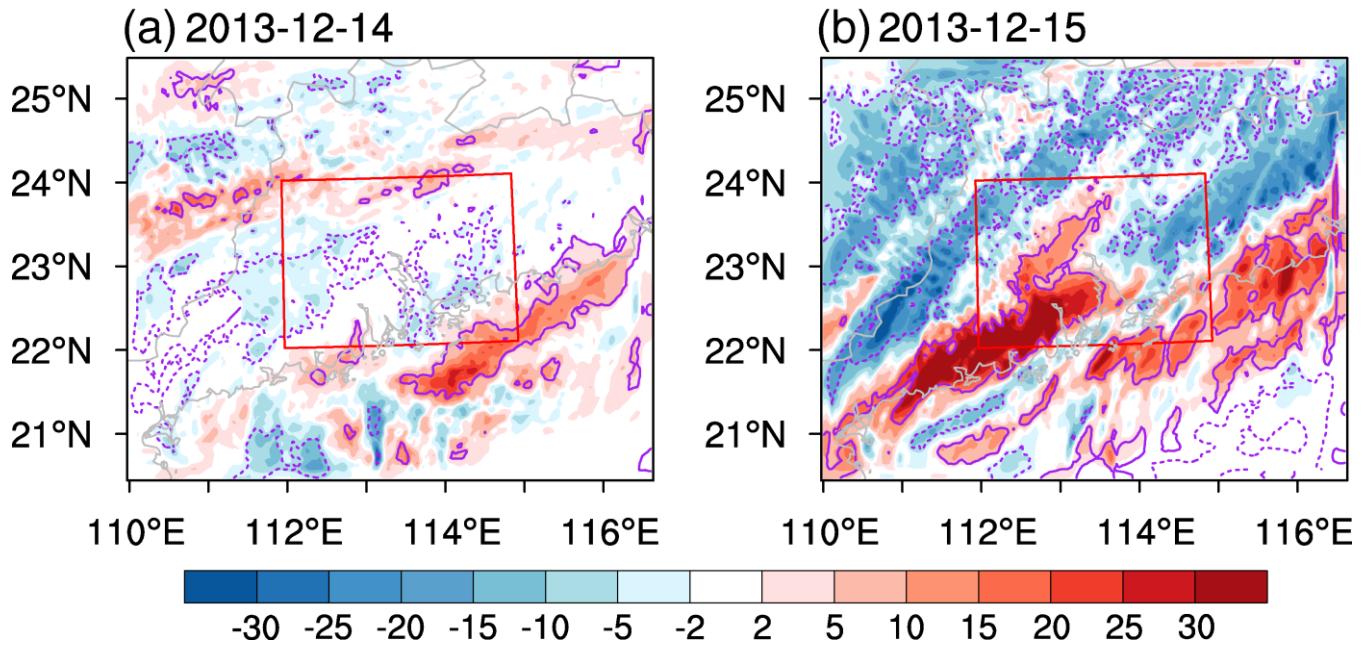
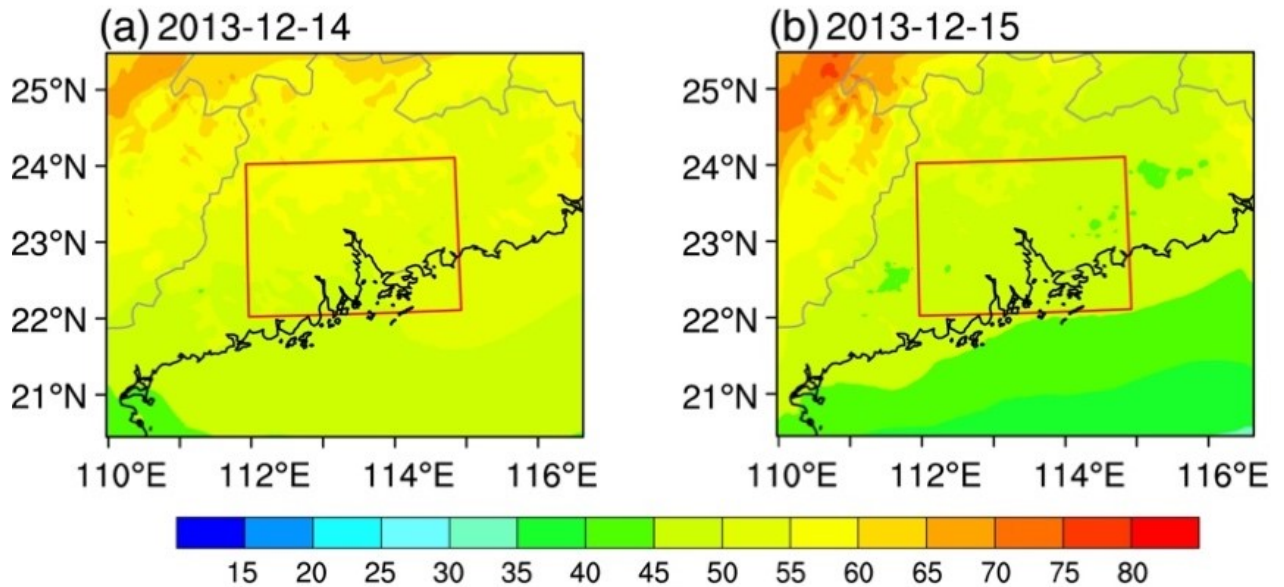
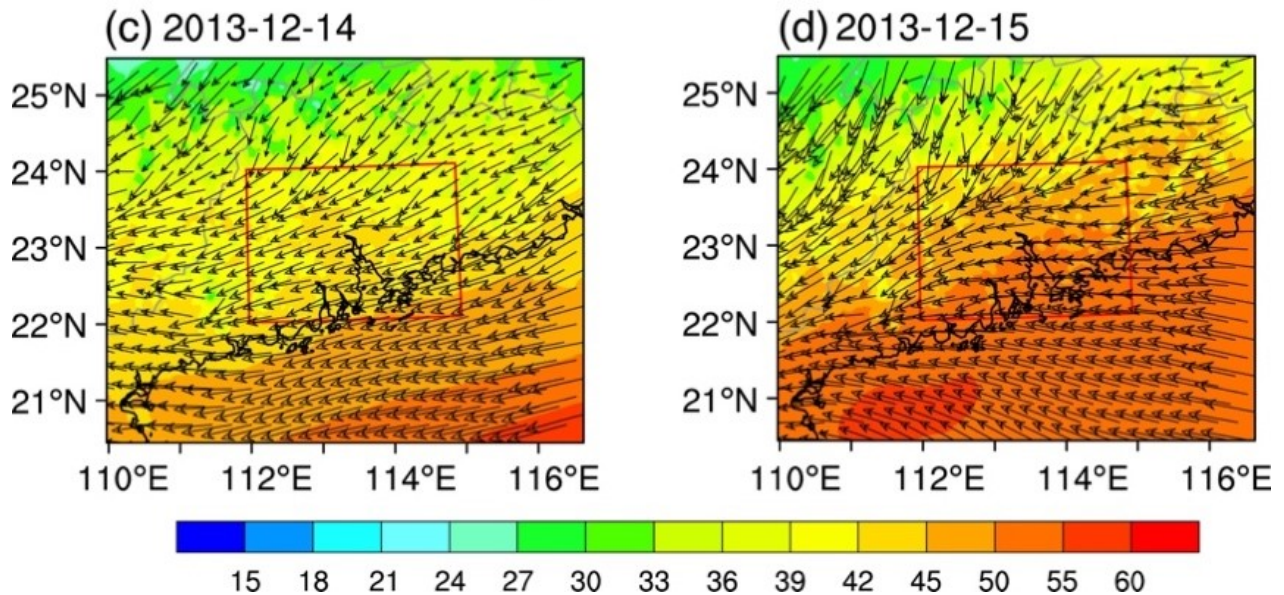


Figure 19. Differences in precipitation (unit: mm) between 10× and CLEAN (i.e., 10× minus CLEAN) on (a) December 14 and (b) December 15. Solid (dashed) purple contour lines indicate positive (negative) differences at the 90% significance according to two-tailed Student's t test. Red boxes (22° – 24° N, 112° – 115° E) denote the analysis region.

Wind Shear



Water Vapor & 925-hPa Wind



5 Figure 20. Spatial distribution of wind shear (unit: m s^{-1}) on (a) December 14 and (b) December 15 in 2013 in the CTL run (first row). Wind shear is calculated as differences between maximum wind speed and minimum wind speed at 0–10 km. Spatial distribution of column-integrated water vapor (shading; unit: mm day^{-1}) and 925-hPa wind (vector; unit: m s^{-1}) on (c) December 14 and (d) December 15 in 2013 in CTL (second row). Red boxes (22° – 24° N, 112° – 115° E) denote the analysis region.

5 **Table 1. Model simulations. Abbreviations: CTL, control run; ARIoff, turn off aerosol-radiation interactions; D1, keep emissions in domain 1 as control run while make those except for chemical boundary conditions in domain 2 as CLEAN run; D2, keep emissions and chemical initial conditions in domain 2 as control run, make those and chemical boundary conditions in domain 1 as CLEAN run; 10 \times , tenfold of anthropogenic emissions and chemical initial and boundary conditions. * indicates that emissions, initial conditions (ICs), or boundary conditions (BCs), are scaled from the control run. Note the offline chemical BCs here were extracted from global chemical transport models and only used for domain 1.**

Simulation	Anthropogenic and fire emissions, chemical ICs and BCs*		Aerosol-radiation interactions	Aerosol-cloud interactions
	Domain 1	Domain 2		
CTL	1	1	Yes	Yes
ARIoff	1	1	No	Yes
CLEAN	0.1	0.1	Yes	Yes
D1	1	0.1	Yes	Yes
D2	0.1	1	Yes	Yes
10 \times	10	10	Yes	Yes